Energy performance of Cutter Soil Mix energy walls

A numerical modelling study

Gerola, Marco; Leclercq, Vincent; Vardon, Philip J.; Cecinato, Francesco

DOI
10.1016/j.tust.2025.106843

Publication date
2025

Document Version
Final published version

Published in
Tunnelling and Underground Space Technology

Tunnelling and Underground Space Technology 165 (2025) 106843

Contents lists available at ScienceDirect

Tunnelling and Underground Space Technology

journal homepage: www.elsevier.com/locate/tust

Energy performance of Cutter Soil Mix energy walls: A numerical modelling study

Marco Gerola [a,*], Vincent Leclercq [b], Philip J. Vardon [c], Francesco Cecinato [a]

[a] Dipartimento di Scienze della Terra'A. Desio', Università degli studi di Milano, Via Luigi Mangiagalli, 34, Milano, 20133, Italy
[b] CRUX Engineering BV, Phoenixstraat 28c, Delft, 2611 AL, The Netherlands
[c] Geo-Engineering Section, Delft University of Technology, PO Box 5048, Delft, 2600 GA, The Netherlands

ARTICLE INFO

Keywords:
Cutter soil mix
Energy wall
Diaphragm wall
Energy geostructures
Shallow geothermal energy

ABSTRACT

The Cutter Soil Mix (CSM) energy wall represents a novel type of energy geostructure, merging the environmental and cost benefits of the CSM technique with ground source heat pump technology. This innovation necessitated comprehensive research to understand the thermal, physical and mechanical characteristics of the material, and optimise energy performance of the CSM energy wall. Laboratory tests and finite element numerical modelling, replicating a full-scale CSM test site in Amstelveen (the Netherlands), were employed to evaluate energy performance under varying demand scenarios: heating only, and combined heating and cooling. Key aspects examined include the influence of horizontal connection pipes on energy extraction and injection, and the impact of U-loop configuration on heat exchange rates over short and long terms. Findings indicate that energy demand significantly affects system performance, with combined heating and cooling demands enhancing long-term heat exchange rates compared to heating-only scenarios. The study demonstrates that non-insulated connection pipes increase overall heat exchange rates, especially under heating-only conditions, while reducing the number of U-loops decreases thermal interaction and enhances energy extraction rates per activated area.

1. Introduction

In recent decades, the drive to reduce fossil fuel dependence has significantly increased the use of shallow ground source heating and cooling installations, which support low-temperature heating and cooling systems. As a result, ground source heat pump (GSHP) systems are expected to play a major role in providing renewable energy sources (Lund et al., 2011; Sanner, 2019).

GSHP systems consist of a series of ground heat exchangers forming the primary circuit and a building heating system as the secondary circuit. The main capital costs of these systems are associated with the heat pumps and the installation of ground heat exchangers, which involves placing pipes into the ground. To mitigate the installation cost, one approach is to use energy geostructures (EGs). EGs are geotechnical structures embedded in the ground that primarily serve a structural function. Additionally, they are thermally active, incorporating heat exchanger pipes to utilise the subsoil for heat dissipation in summer and/or heat extraction in winter (Brandl, 2006).

The most common type of EG is the energy pile (Amatya et al., 2012), but current research also focuses on other underground structural elements embedding heat exchangers, such as energy tunnels, ground anchors, and diaphragm walls (Adam and Markiewicz, 2009; Mimouni et al., 2013). Diaphragm energy walls, in particular, represent a promising technology due to their large surface area, which can be thermally activated through various pipe configurations (Kürten et al., 2015; Makasis and Narsilio, 2020). These walls are widely used in urban excavations for building basements, parking structures, and underground works constructed using the cut-and-cover method.

When compared to other EGs such as energy piles, energy walls are relatively new (Sun et al., 2013). The first thermally activated energy wall was constructed in 1996 in Austria (Brandl, 2006). Since then, they have been installed at a limited number of locations, including the Bulgari Hotel in the UK (Amis et al., 2010), a new railway line in London (Amis and Loveridge, 2014), a residential building in Northern Italy (Angelotti and Sterpi, 2018), and the Museum of Natural History in China (Xia et al., 2012).

The thermal behaviour of energy walls is inherently complex due to their planar geometry, which distinguishes them from other energy geostructures (Sterpi et al., 2017). Various studies have reported a range of heat exchange rates, typically between 10–50 W/m^2 (Di Donna et al., 2017a; Zannin et al., 2021), 20–40 W/m^2 (Laloui and Sutman,

* Corresponding author.
E-mail address: marco.gerola@unimi.it (M. Gerola).

https://doi.org/10.1016/j.tust.2025.106843
Received 28 August 2024; Received in revised form 21 June 2025; Accepted 29 June 2025
Available online 22 July 2025

2019), and 15–25 W/m^2 (Di Donna et al., 2021). This wide range is influenced by multiple factors, including pipe spacing, groundwater flow, concrete thermal conductivity, and the temperature differential between the air inside the excavation and the surrounding soil (Di Donna et al., 2017b). Furthermore, in systems dominated by unidirectional heat transfer, where heat is either consistently extracted from or injected into the ground, the performance tends to decrease over time. This is in contrast to systems operating with seasonal variations in heat extraction and injection, which maintain higher performance levels over extended periods (Loveridge et al., 2020).

Cutter Soil Mixing (CSM) is an innovative technique for constructing cut-off and retaining walls. This method involves in situ mixing of soil with a cementitious binder slurry using specialised mixing tools, creating a mortar-like material in which soil particles serve as aggregates. Unlike conventional mortar or concrete, soil–cement mortar produced by CSM may lack uniform composition, particularly in terms of aggregates, due to natural limitations and the less controlled conditions of in-situ soil mixing (Arnold et al., 2011). The CSM tool cuts vertical rectangular panels making it particularly suitable for linear in-situ structures such as cut-off barriers, retaining walls, and liquefaction mitigation cells (Topolnicki, 2016). When additional strength or resistance to bending moments is required, the CSM wall can be effectively reinforced with steel sections or cages (Fiorotto et al., 2005). Two key advantages of the CSM method are the reduce need of transporting and purchasing aggregates, achieved by utilising in-situ soil as a primary construction material, and its low vibration impact, making it particularly suitable for implementation in densely built urban areas. The volume of excavated material and spoil requiring treatment, transport, and off-site disposal is significantly diminished, contingent upon ground conditions. This technique is both environmentally friendly and economical, providing higher performance compared to two-phase cut-off walls or secant pile walls, where soil must be excavated and subsequently filled, often under water or with a supporting fluid.

Combining energy wall technology with the CSM technique leverages the environmental and cost advantages of both methods. To gain deeper insights into the thermal behaviour of a CSM energy wall installation, a full-scale CSM test site was developed in Amstelveen, The Netherlands (Leclercq et al., 2023). The CSM wall served dual purposes: acting as a hydrological barrier during the construction phase and as a load-bearing foundation for a two-story building. To thermo-activate the CSM wall, a GSHP system was installed. Heat exchanger loops were attached to the steel column profiles embedded within the CSM wall, facilitating the transfer of heat between the ground and the building's heating and cooling systems.

Given the nascent stage of this technology, investigations into its energy performance through numerical modelling are crucial to gain deeper insights into the system's energy performance.

In this study, the energy performance of a full-scale CSM energy wall test installed in Amstelveen (NL) is evaluated through numerical modelling. Initially, computerised tomography, hot disk, and UCS tests were conducted on CSM wall samples from the test site to determine the material's basic thermal and mechanical properties. Subsequently, a Finite Element (FE) numerical model was developed to replicate the full-scale CSM energy wall. This FE model enables a comprehensive and accurate three-dimensional analysis of the heat exchange processes within the CSM. The energy performance is evaluated both in the short and long term under two different energy demand scenarios: one with only heating demand and the other with both heating and cooling demand. Additionally, the FE model assesses the relative influence of the horizontal pipes, which connect the vertical loops to each other or to the main manifold linked to the heat pump, and examines the impact of the hydraulic system setup on the system's short and long-term energy performance.

Table 1
Soil Layers characterisation of the CSM full scale test.

Soil layer	Starting depth [m]
Sand	0.0
Peat	3.0
Clay	4.2
Sand	7.4
Clay	7.9
Peat	10.5
Sand	11.0
Clay	14.8
Sand	15.2

2. Full scale CSM energy wall setup

A two-story building is currently under construction in Amstelveen, the Netherlands. Situated within a radius of 5 m from any neighbouring structures, this new edifice will feature a basement level measuring 12.1 m × 20.3 m, with a height of 3.5 m. The building's foundation, which reaches a depth of 17.3 m, is constructed using the CSM wall technique. The CSM wall fulfils three primary functions: (1) it acts as a hydraulic barrier during construction, enabling effective groundwater management within the construction site without significantly altering groundwater level outside the site's perimeter; (2) it serves as a soil-retaining structure for the excavation site, ensuring stability; and (3) it provides a load-bearing foundation for the structure upon completion. The CSM wall installation involves separate, adjacent panels (each with a width of 1.1 m and a thickness of 0.55 m) positioned within the construction pit, serving as permanent foundations.

The CSM wall is surrounded by soil, with the soil layer shown in Table 1, on both sides for a length of 13.8 m. In the more shallow segment where the 3.5 m deep basement is situated, one face of the CSM wall interfaces with soil, while the opposing side interfaces with the interior of the building. Between the CSM wall and the basement internal space, and at the base of the basement cavity, a thermal insulation layer is installed to prevent heat loss from the building's internal environment.

To strengthen the CSM wall, steel IPE300 reinforcement profiles are installed within the CSM wall during its liquid phase to provide an higher load-bearing support for the building. These profiles, characterised by S275 steel, are spaced at intervals of 1.1 m. A total of 62 reinforcement profiles are positioned at the edge, and 12 are located in the diaphragm panels located at the centre of the basement as depicted in Fig. 1. High-density polyethylene (HDPE) heat exchanger pipes with a diameter of 20 mm are attached to the edge steel profiles along their entire length to thermally activate the CSM wall as shown in Fig. 2. To avoid any pipe damages during installation, a plastic protection is installed in protection of the U shape at the bottom of the IPE column, and spacers are attached along the profiles to maintain a consistent distance between the two pipe shanks. To prevent freezing, an 80%–20% water–glycol mixture is utilised as the heat exchange fluid.

As regards the structural design, reinforcement profiles are required up to a depth of 11 m at the edge of the CSM walls and up to 8 m in the centre of the basement. To enhance thermal extraction, the external reinforcement profiles, along with attached bottom loops, extend to a depth of 14.9 m. A total of 52 U-loops are attached to the steel profiles: 40 with a depth of 14.3 m and 12 with a depth of 10.3 m. This configuration serves to assess the energy extraction rate from the deeper sand layer shown in Table 1, which solely interfaces with the deeper heat exchanger pipes.

The reinforcement profiles are installed to a depth of 14.9 m, while the CSM wall extends to a total length of 17.3 m. This extended length serves a dual purpose: functioning as a hydraulic barrier and enhancing wall stability by anchoring its toe into the sand layer, which begins at a depth of 15.2 m. The portion of the soil-mixed wall beyond the

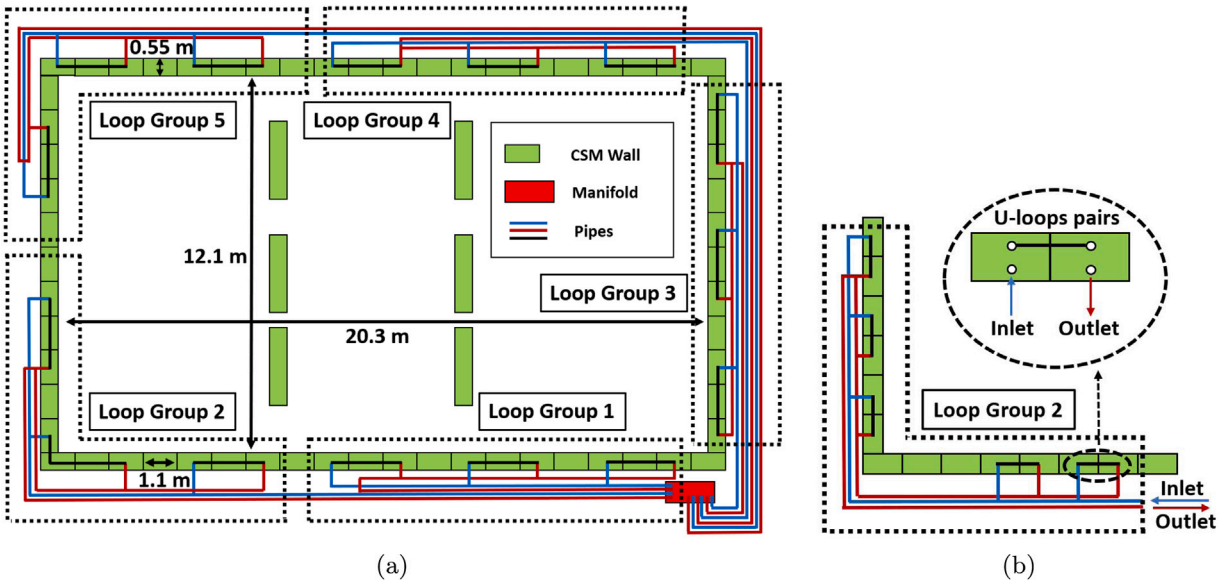

Fig. 1. CSM energy wall full-scale test hydraulic system setup: (a) loop groups overview, and (b) loop group 2 details.

Fig. 2. CSM full-scale test installed in Amstelveen (NL): (a) heat exchanger pipes on the steel IPE300 profiles, and (b) CSM energy wall full scale test.

reinforcement depth remains unreinforced. The additional length of the soil mix wall is left unarmed.

The hydraulic system (Fig. 1) comprises five groups of pipes arranged in parallel. The loop groups 1, 2, 3 and 4 contain deeper loops and include a total of 10 U-loops, and loop group 5, that comprises shallower loops, consists of 12 U-loops. Within each group, U-loops are connected in series in pairs, forming parallel configurations of two U-loops each as shown in Fig. 1 for loop group 2.

In each group, there are two main pipes: one connected the first U-loop of each pair and the manifold, where the heat pump pipes are connected. The second primary pipe aggregates the output from all pairs within the subgroup, channelling it back to the manifold.

3. Laboratory tests and results

3.1. Samples

A total of 11 cylindrical samples, each with a diameter of 10 cm, were extracted from two distinct vertical sections of the CSM walls for laboratory testing. Initially, all samples underwent computerised

Table 2
Samples used for unconfined compression test characteristics.

Sample name	Vertical section	Starting depth [cm]	Height [cm]	Density [kg/m^3]	Original soil layer
UC1	1	138	20.8	1716	Sand
UC2	1	164	20.7	1659	Sand
UC3	1	238	20.9	1809	Sand
UC4	1	430	20.7	1716	Organic clay
UC5	1	836	20.9	1706	Organic clay
UC6	1	859	20.6	1706	Organic clay
UC7	1	1233	20.5	1767	Sand
UC8	2	930	20.7	1769	Organic clay
UC9	2	1135	20.8	1787	Sand
UC10	2	1161	20.6	1741	Sand
UC11	2	1240	20.5	1748	Sand

tomography (CT) scanning. Subsequently, these samples were cut to produce 11 specimens, each 20 cm in height, suitable for unconfined compression (UC) tests, and 15 smaller specimens for thermal conductivity assessments using the hot disk (HD) method, to evaluate their unconfined compression strength (UCS) and thermal properties such as thermal conductivity and heat capacity. The vertical section, starting depths, heights, densities, and the original soil layers corresponding to the sampling depth are detailed in Table 2 for the UC specimens.

After cutting, each sample had a well-defined cylindrical form, and both volume and mass were measured to determine the density of the specimens. The average measured density was calculated at 1738 kg/m^3 with a standard deviation of 43 kg/m^3. The average density of samples extracted from the clay layer was 1724 kg/m^3, slightly smaller than those from the sand layer, which averaged 1746 kg/m^3. Overall, the limited standard deviation across the samples indicates a rather uniform density distribution. These measurements lie between the density of the fluid cement used (approximately 2400 kg/m^3) and the densities of the original soil layers (1600 kg/m^3 for organic clay and 1800 kg/m^3 for sand). It is worth noting that no data are available regarding the saturation degree and water content of the samples, and it is likely that a reduction in density, due to partial drying, occurred between the sampling and measurement phases.

The homogeneity in density across different depths suggests high mixing among the different soil layers and concrete. Furthermore, the average density being closer to that of the soil than to that of concrete suggests that the proportion of fluid concrete mixed with the soil during the CSM wall construction was relatively low compared to the volume of soil incorporated into the mix.

3.2. Computerised tomography

To enhance the understanding of the material composition of the CSM wall, CT scans were conducted on all samples. CT scanning is a diagnostic imaging technique that employs a combination of X-rays and computer technology to generate detailed cross-section images (at intervals of 0.6 mm for the case at hand) of the sample under analysis.

During CT image reconstruction, the absorption or attenuation coefficient of radiation within a material is utilised to evaluate the physical density of the material through the calculation of the Hounsfield Unit (HU). In HU scale, distilled water at standard temperature and pressure is assigned a value of zero HU, air is set at −1000 HU, and denser materials are given positive values, while those less dense than water receive negative values (e.g. see Broder and Preston (2011)). To convert HU values to actual bulk density measurements in kg/m^3, a linear interpolation is employed based on established reference points: 0 HU corresponds to the density of water (1000 kg/m^3), and −1000 HU corresponds to the density of air (0 kg/m^3):

$$Density = HU + 1000 \quad (1)$$

Each pixel in the CT scan images is assigned a HU and corresponds to a spatial resolution of 0.3 mm × 0.3 mm. These HU values are considered constant over a depth of 0.6 mm, which is the distance between two consecutive cross-sectional images obtained from the scan. The size of the pixel is larger than the grain size of organic clay, which is typically less than 0.002 mm, but it is on the same order of magnitude as the grain size of sand, which ranges from 0.06 mm to 2 mm. Consequently, the density values estimated from CT scanning should be considered as representing the bulk density for the organic clay, given that the pixel dimensions are larger than the grain size of the soil. For the sandy soil, the estimated density values may range between the bulk density and the particle density. Despite these differences in scale relative to particle size, the overall density of each sample is calculated by averaging the values across each cross-section, leading to a final measurement that is considered representative of the bulk density of the sample. Fig. 3 illustrates a comparison between an actual photograph of a sample section and its corresponding image obtained from a CT scan.

In Table 3, a comparison is presented between the densities computed from CT scan data and those measured directly by assessing the volume and weight of the cylindrical samples utilised in UC tests. The comparative analysis yields an average difference of 6.8%, indicating a good agreement between the results. Specifically, the densities derived from the CT scans are observed to be consistently higher than those measured directly. The observed discrepancy could be attributed to variations in water content within the samples at the time of scanning, which was not quantified. Partial drying of the material may have started from the day of sampling: Fig. 3 displays a computerised cross-section where the boundaries exhibit lower densities, likely indicative of reduced water content. Similarly, Fig. 4 presents a vertical cross-sectional slice where the lower part of the section shows lower density. This further decrease in water content is plausible given that the CT scans were performed few weeks prior to the subsequent measurements of weight and volume, allowing time for moisture loss. Notably, the samples displaying the greatest discrepancies, specifically UC2 and UC6, were those for which the longest intervals elapsed between CT scanning and the subsequent weight and volume measurements. It is worth noting that the assumption of linear interpolation between the HU and material density represents a simplification, which may contribute to the discrepancies observed in the data.

Utilising density estimations derived from CT scans enables the assessment of density distribution within the samples. To mitigate potential inaccuracies arising from disparities between measured and computed densities, density ranges are selected to provide a broad overview: ranging from 0 kg/m^3 to 500 kg/m^3 to identify macro pores and very low-density material fractions, from 500 kg/m^3 to 1400 kg/m^3 for low-density materials, 1400 kg/m^3 to 1800 kg/m^3 corresponding to the bulk density of organic clay, with values exceeding 1800 kg/m^3 representing to the bulk density of sand and high-density materials such as cement mixed with the soil in the CSM wall. The distribution of these density ranges across each sample is detailed in Table 4.

Materials with a density lower than 500 kg/m^3, including macro pores, account for less than 1% of the volume in all the samples. In contrast, the density range exceeding 1800 kg/m^3, primarily associated with sand and concrete, constitutes more than 80% of the total

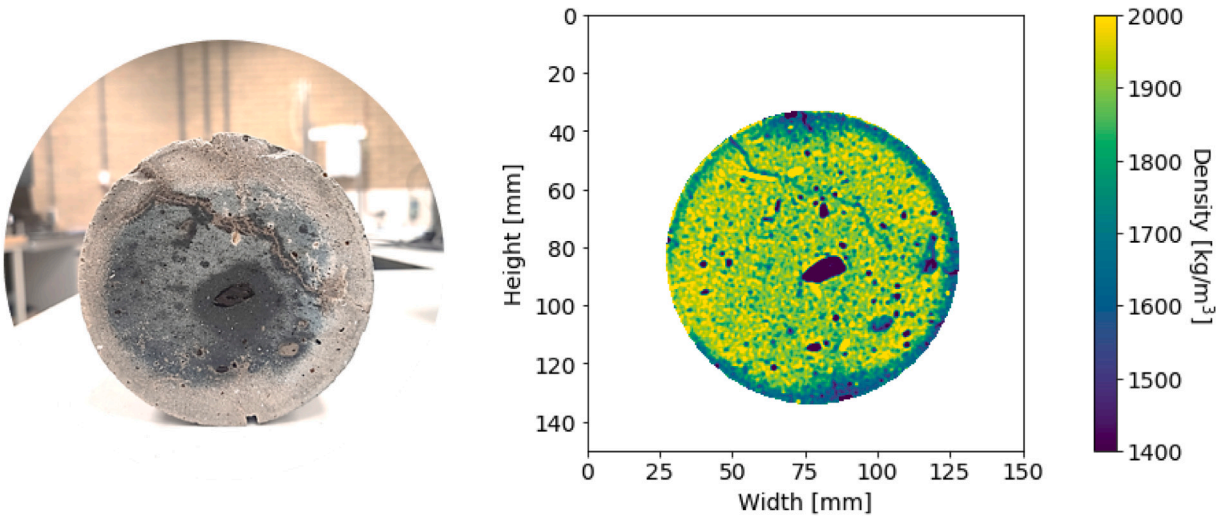

Fig. 3. Comparison between a real cross section and the corresponding processed image from CT scan test of the UC2 sample.

Table 3
Comparison between the computed and measured density for the UC samples.

Sample name	Weight [g]	Measured density [kg/m^3]	Computed density [kg/m^3]	Difference %
UC1	2804	1716	1850	7.2
UC2	2697	1659	1872	11.4
UC3	2969	1809	1896	4.6
UC4	2790	1716	1823	5.9
UC5	2800	1706	1837	7.1
UC6	2761	1706	1861	8.3
UC7	2845	1767	1866	5.3
UC8	2876	1769	1878	5.8
UC9	2920	1787	1902	6.0
UC10	2816	1741	1872	7.0
UC11	2815	1748	1857	5.9
Average	2826	1738	1865	6.8

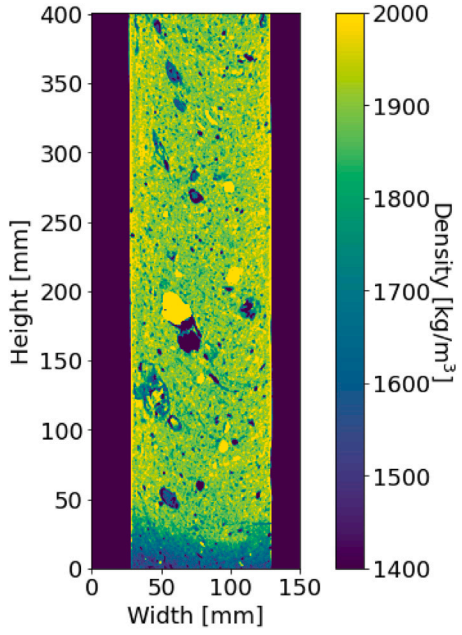

Fig. 4. Computerised vertical section of the sample UC4.

density in almost all samples. Notably, samples originating from the organic clay layer exhibit 6.6% less mass volume of material within the >1800 kg/m^3 range and 6.4% more mass volume within the 1400–1800 kg/m^3 range compared to the average observed in sand samples, likely due to the presence of more clay material.

3.3. Hot disk

A total of 15 specimens were tested with the hot disk to evaluate their thermal conductivity and volumetric heat capacity that are shown in Table 5. The average thermal conductivity was found to be 0.95 W/mK, and the average volumetric heat capacity was 2.79 MJ/m^{3}K, both exhibiting low standard deviations of 0.09 W/mK and 0.23 MJ/m^{3}K, respectively, reflecting consistency across the samples. The measured values for thermal conductivity and heat capacity fall within the expected range for partially saturated clay and medium sand Dalla Santa et al. (2020). Thermal conductivity values exceed those typically associated with peat, while heat capacity values are lower, supporting the minimal influence of peat on the thermal properties of the CSM samples as outlined in Section 3.2. Additionally, the thermal conductivity is situated at the lower boundary of the range characteristic for concrete (Laloui and Rotta Loria, 2019). These findings highlight the predominant influence of soil type over concrete content on the thermal characteristics of the samples, likely due to a high soil-to-concrete ratio within the CSM wall.

The majority of the tested specimens consisted of CSM material derived from an original sand layer while only one is from an original

Table 4
Density composition for the UC samples.

Sample name	Density range				
	0–500 [kg/m^3] %	500–1400 [kg/m^3] %	1400–1800 [kg/m^3] %	>1800 [kg/m^3] %	Soil layer %
UC1	0.2	1.5	18.1	80.1	Sand
UC2	0.2	1.3	12.7	85.9	Sand
UC3	0.3	1.7	14.2	83.8	Sand
UC4	0.6	1.7	21.2	76.4	Organic Clay
UC5	0.3	1.7	18.9	79.1	Organic Clay
UC6	0.3	1.9	26.1	71.7	Organic Clay
UC7	0.4	1.5	13.4	84.7	Sand
UC8	0.3	1.4	14.4	83.8	Organic Clay
UC9	0.2	1.3	10.0	88.6	Sand
UC10	0.3	1.9	15.1	82.7	Sand
UC11	0.3	1.4	13.4	84.9	Sand
Total average	0.3	1.6	16.1	82.0	
Sand average	0.3	1.5	13.8	84.4	
Clay average	0.4	1.7	20.2	77.8	

Table 5
Density and thermal properties of the HD samples.

Sample name	Measured density [kg/m^3]	Thermal conductivity [W/mK]	Heat capacity [MJ/m^{3}K]	Soil layer
HD1	/	0.86	2.85	Sand
HD2	1705	0.97	2.85	Sand
HD3	1707	0.93	2.55	Sand
HD4	/	0.82	2.54	Sand
HD5	/	1.03	2.88	Sand
HD6	1747	1.07	2.96	Sand
HD7	/	0.94	2.74	Sand
HD8	/	1.00	3.21	Organic clay
HD9	/	1.09	2.44	Sand
HD10	1673	0.96	2.87	Sand
HD11	/	0.75	2.61	Sand
HD12	/	0.97	3.20	Sand
HD13	1745	1.05	2.57	Sand
HD14	1695	0.92	2.68	Sand
HD15	/	0.90	2.79	Sand
Average	1703	0.95	2.79	
Standard deviation	83	0.09	0.23	

Table 6
Unconfined compression strength values.

Sample name	Unconfined compression strength [MPa]
UC1	9.1
UC2	9.6
UC3	8.1
UC4	7.8
UC5	9.3
UC6	10.1
UC7	10.1
UC8	9.6
UC9	9.5
UC10	7.5
UC11	10.9
Average	9.2
Sand average	9.2
Clay average	9.2

organic clay layer. Consequently, it is not feasible to establish possible correlations between the original soil layers and the thermal properties of the specimens due to the limited diversity in substrate types.

The reduced water content in the CSM samples relative to the in situ CSM material, as discussed in Section 3.2, may result in an underestimation of density, thermal conductivity and heat capacity. Hence, employing these parameters to evaluate the energy performance of the CSM energy wall is likely to yield conservative outcomes.

3.4. Unconfined compression test

A series of UC tests were conducted on the CSM material samples. The axial stress versus vertical displacement, plotted up to the maximum stress corresponding to the UCS values, is depicted in Fig. 5 for the 11 specimens listed in Table 4. The average UCS values, presented in Table 6, average 9.2 MPa across all samples with a standard deviation of 1 MPa. This value remains consistent when considering specimens solely from sand or organic clay layers, indicating uniform UCS values despite variations in the original soil layers. Additionally, most samples exhibit consistent pre-rupture pseudo-elastic behaviour.

No direct correlations could be established between UCS values and either density or material composition. The variability in UC test results is most likely linked to pre-existing small cracks in the samples, which were related to the sampling technique and exacerbated by changes in water content post-sampling.

4. Numerical model

A FE numerical model was developed using COMSOL Multiphysics software to conduct a comprehensive analysis of the thermal behaviour and energy performance of the CSM system. This FE model is utilised to evaluate the system's performance under various scenarios, including different heating and cooling demands, configurations of heat exchanger pipes, and the presence or absence of insulation on the connection pipes.

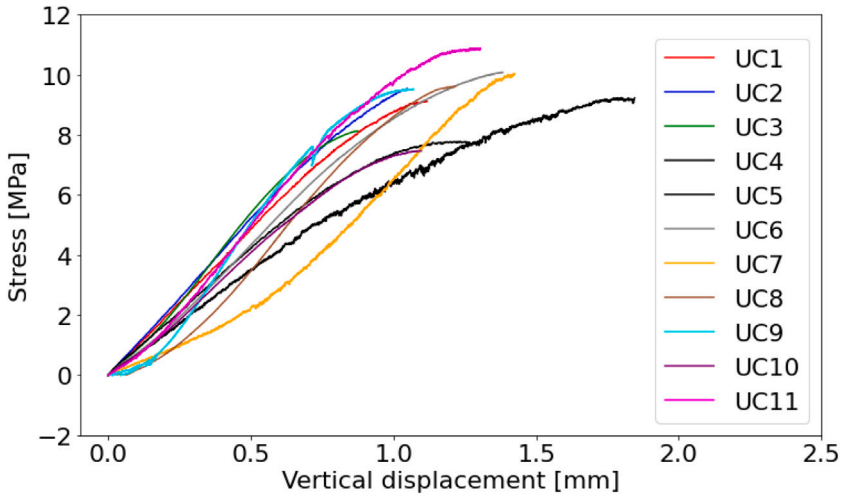

Fig. 5. Unconfined compression test results.

4.1. Governing equations

The proposed numerical model simulates the primary heat transfer processes occurring within the CSM and adjacent materials. In the geothermal system at hand, heat exchange is primarily governed by conduction and convection. Convection predominates in the transfer of heat between the heat carrier fluid and the HDPE pipe walls, whereas conduction regulates the heat interactions within the CSM wall and the soil materials. Additional thermal phenomena such as thermal radiation at the soil surface and convective heat transfer in pore water due to groundwater movement may also occur. However, radiant heat exchange is generally minimal except in the coarsest soils (Rees et al., 2000; Fillion et al., 2011), and the potential for groundwater convection is low at the field test site.

The heat conduction process within the system is described by the transient heat diffusion equation, as outlined in Lewis and Schrefler (1998). When integrating the convection process, the transient heat equation is formulated as:

$$\rho C_p \frac{\partial T}{\partial t} + \rho C_p \mathbf{u} \cdot \nabla T + \nabla \cdot q = Q_{\text{wall}} \tag{2}$$

here, ρ is the density of the material [kg/m^3], C_p is the specific heat capacity at constant pressure of the fluid [J/kgK], T denotes temperature [K], t represents time [s], $\mathbf{u}$ is the fluid velocity [m/s]. $q = -\lambda \nabla T$ represents the heat flux vector, in accordance with Fourier's law and Q_{wall} is the heat or sink source term, employed to couple the heat extraction from the heat exchanger pipes.

To model thermal energy transfer within the pipes, a one-dimensional approach is applied by integrating the momentum conservation and mass conservation equations into the energy balance equation. This provides a simplified depiction of fluid flow and heat transfer dynamics:

$$A_p \rho_f C_p \frac{\partial T}{\partial t} + A_p \rho_f C_p \mathbf{u_p} \cdot \nabla T = \nabla (A_p \lambda_f \nabla T) + f_D \frac{\rho_f A_p}{2 d_h} |\mathbf{u_p}|^3 + q'_{\text{wall}} \tag{3}$$

where mA_p is the pipe cross-section of the heat exchanger pipes [m^2], ρ_f denotes the fluid density [kg/m^3], $\mathbf{u_p}$ represents the average fluid velocity along the tangent of the centre line of the pipes [m/s]. The term $q'_{\text{wall}} = -Q_{\text{wall}} A_p$ quantifies the radial heat flux across the pipe walls. This flux is computed using the equation $Q_{\text{wall}} = (hZ)_{\text{eff}}(T_{\text{ext}} - T)$, where h represents the effective heat transfer coefficient, Z denotes the perimeter of the pipe, and T_{ext} is the external temperature surrounding the pipe. Additional information regarding the calculation of the effective heat transfer coefficient h can be found in COMSOL (2021). In Eq. (3), the second term on the right-hand side quantifies the heat dissipation due to internal friction within the fluid, representing energy losses attributable to viscous effects and fluid motion within the pipes.

4.2. Numerical model description

The numerical model was developed primarily to assess the energy performance of the CSM energy wall in various scenarios involving both heating and cooling demands. The model domain is parallelepipedal in shape, measuring 43 m in width, 51 m in length, and 20 m in height, as illustrated in Fig. 6(a). The building's basement, which measures 3.5 m in depth, 12.1 m in width, and 20.3 m in length, is excluded from the model domain. The CSM wall, located in the middle of the FE model, extends to a depth of 17.3 m.

The heat exchanger loops, which are a key feature of the CSM case study depicted in Fig. 6(b), are integrated into the model using a 1-D simplification approach described in Section 4.1 and in Gerola et al. (2023). These loops, made of HDPE, are arranged both vertically (U-loops) and horizontally (connection pipes). The horizontal pipes, buried at a depth of 0.8 m, link the vertical U-loops to the secondary circuit (not explicitly simulated but represented by the inlet temperature boundary condition) and to each other. The configuration of the heat exchanger pipes mirrors the actual setup described in Section 2 and depicted in Fig. 1. The simulation does not incorporate the steel reinforcement profiles due to their relatively small scale compared to the extensive dimensions of the model domain. Consequently, the CSM wall is modelled as a homogeneous material throughout its entire volume.

The model domain is divided into different soil layers, each characterised by distinct properties as delineated in Table 7. This Table also includes the properties of the CSM used in the model, based on averages derived from analyses in Section 3. To improve mesh quality and reduce computational time, soil layers with a thickness of 0.5 m or less are not simulated in the numerical model. Soil density, heat capacity, and thermal conductivity were determined using empirical correlations from cone penetrometer test results near the CSM (Vardon and Peuchen, 2021). These values were validated by comparing them with existing geological data (Dalla Santa et al., 2020). These bulk thermal properties were assigned to the solid domain elements within the model. The HDPE material of the pipes is assigned a thermal conductivity of 0.4 W/mK and a wall thickness of 2 mm. The heat exchanger fluid, a mixture comprising 80% water and 20% glycol to lower the freezing point, was modelled with the following properties: thermal conductivity of 0.48 W/mK, specific heat capacity of 3691 J/kgK, density of 1040 kg/m^3, and dynamic viscosity of 0.002314 Pa s (Di Donna and Laloui, 2015), all assumed constant throughout the simulations.

A tetrahedral mesh was generated to refine the mesh near the EQW within the model domain while allowing for a coarser mesh near the

Table 7
Soil layers characterisation.

Soil type	Thickness [m]	Bulk density [kg/m^3]	Thermal conductivity [W/mK]	Specific heat capacity [J/kgK]
Sand	3.0	1800	2.2	1300
Peat	0.8	1050	0.8	2800
Peaty clay	3.7	1650	1	1300
Silty clay	3.1	1800	1.7	1400
Sand	9.0	1800	2.4	1400
CSM	–	1738	0.95	1605

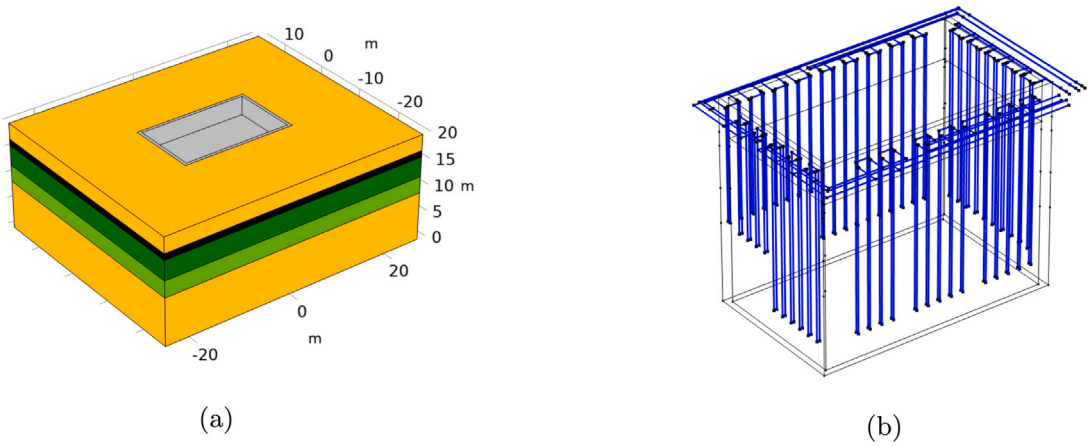

Fig. 6. Details of the numerical model implemented to simulate the thermal exchange processes of the CSM energy wall: (a) Model domain with the soil layers division, and (b) heat exchanger pipes modelled using 1-D line elements.

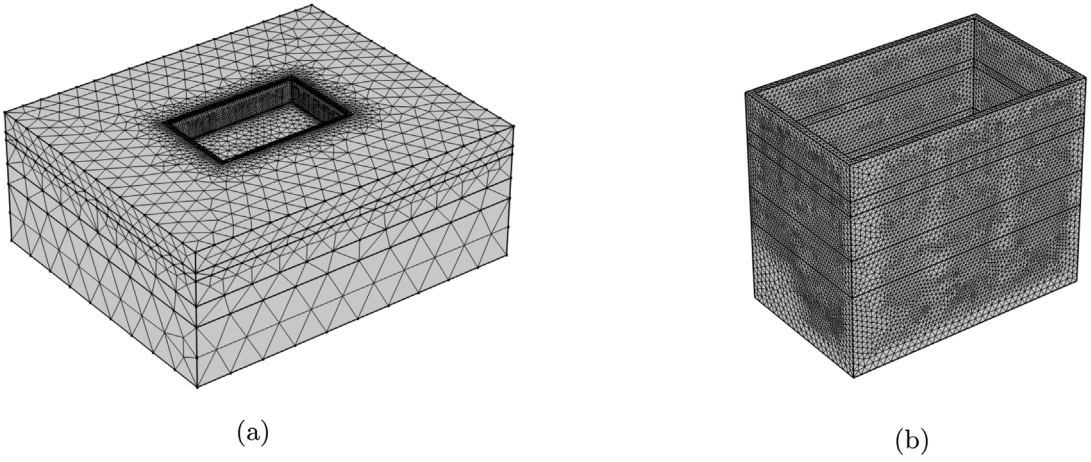

Fig. 7. Mesh elements implemented in the CSM numerical model: (a) model domain, and (b) CSM wall.

lateral boundaries. This approach optimises calculation accuracy near the heat exchanger pipes and maintains manageable computational times. The mesh, as depicted in Fig. 7, comprises a total of 447 564 tetrahedral elements, ensuring an adequate level of detail for precise analysis.

The lateral and lower boundaries of the domain were positioned at a considerable distance from the CSM energy wall to ensure that the heat transfer processes associated with the CSM wall were not influenced by boundary conditions. The lower boundary was assigned a constant temperature of 12 °C, representative of the undisturbed subsurface temperature typical in the Netherlands, corroborated by data from adjacent sites (Busby et al., 2011) and consistent with parameters used in similar shallow geothermal system studies in nearby locations (Gerola et al., 2025; Vardon et al., 2025). Thermal insulation was applied to the lateral boundaries, to the CSM surfaces adjacent to the basement (excluded from the model domain), and to the upper surface of the CSM wall in direct contact with the building. The latter two simulate the thermal insulation layer installed between the basement and the CSM wall.

To account for daily and seasonal variations in air temperature, the daily average temperature, measured at a weather station located 6 km away from the CSM full-scale test location over an eight-year span, was applied to the upper boundary surfaces, excluding those of the CSM. The various boundary conditions implemented within the model are shown in Fig. 8.

To activate the GSHP system within the numerical model, a non-zero velocity and a specified inlet temperature are set as boundary conditions at the inlet pipes. For heating demand, an inlet temperature of 0 °C is assigned to prevent soil freezing whilst ensuring significant heat exchange. Conversely, to simulate cooling demand and maintain water temperatures between 11 °C and 19 °C above the ambient ground temperature of 12 °C to optimise the performance of the GSHP

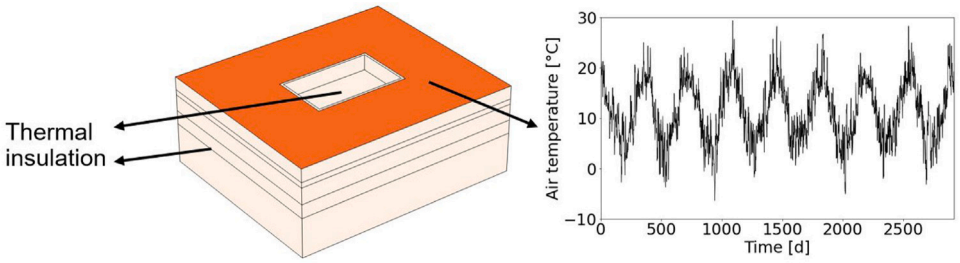

Fig. 8. Boundary conditions of the numerical models.

system (Kavanaugh, 2010), an inlet temperature of 25°C is used. The velocity within the heat exchanger pipes is established at 0.2 m/s, consistent with the flow velocity set for the full-scale test. Further details on the energy demand are provided in Section 5.

The initial temperature profile within the soil was determined using the Hillel function (Hillel, 1982), based on recorded air temperatures and the average thermal properties of the different soil layers.

The simulation of the energy CSM wall's geothermal operation covered an 8-year period and was conducted using a maximum timestep of 1 day. Numerical testing indicated that smaller mesh elements and a reduced maximum timestep would not alter the results. Therefore, these settings were chosen to optimise the balance between computational efficiency and accuracy. The required computational time for one simulation was about 7 h for a workstation with a processor Intel(R) Xeon(R) W-1350P 4.00 GHz 6 cores.

5. Energy demand

The energy demand (ED) of a building for air conditioning in summer and heating in winter is influenced by external temperature, but this relationship is nonlinear (Lee and Chiu, 2011). A common method to quantify this relationship is through the use of degree-day indices calculated daily (Scapin et al., 2016). Degree days represent the difference in degrees Celsius from a reference temperature and quantify the extent to which the average outdoor temperature (T_{ext}) exceeds or falls below a designated threshold. Essentially, degree days measure the amount of heat required to be removed from or supplied to a building to maintain comfortable indoor conditions, categorised as cooling degree days (CDD) and heating degree days (HDD), respectively. The calculations for HDD and CDD are expressed as follows:

$$HDD = \max(T^* - T_{ext}, 0) \tag{4}$$

$$CDD = \max(T_{ext} - T^{**}, 0) \tag{5}$$

where T^* and T^{**} represent the threshold temperatures for HDD and CDD, respectively. These thresholds vary according to climate and geographical location. For instance, in Italy, thresholds of 18 °C and 21 °C are utilised for HDD and CDD, respectively (Adinolfi et al., 2020), while other studies employ 17 °C and 22 °C (Petralli et al., 2011). In Croatia, CDD evaluations use thresholds of 18 °C, 21 °C, and 23 °C . A unified threshold of 18 °C has also been suggested for evaluating both HDD and CDD (Cvitan and Jurković, 2016). In Greece, the bases for HDD are set at 14 °C, 15 °C, and 18 °C, and for CDD at 24 °C and 26°C (Moustris et al., 2015; Matzarakis and Balafoutis, 2004; Papakostas et al., 2010). To evaluate the ED related to the CSM full scale test, the base temperatures for HDD (T^*) and CDD (T^{**}) are set at 15.5 °C and 18 °C, respectively.

The ED of a building is determined based on the monthly sum of the HDD and CDD values using the following thresholds (Adinolfi et al., 2020):

- If the monthly sum of HDD or CDD is less than 70 °C, the building requires neither air conditioning nor heating, and the GSHP system remains inactive with no energy extraction.
- If the monthly sum of HDD or CDD ranges between 70 °C and 130 °C, the GSHP system operates intermittently, functioning for half of the month and remaining off for the other half.
- If the monthly sum of HDD or CDD exceeds 130 °C, the GSHP system operates continuously throughout the month.

HDD and CDD were calculated using temperature data spanning from 2015 to 2023. To assess the energy performance of the system for both heating and cooling demands, the minimum and maximum recorded daily temperatures were utilised. Fig. 9(a) illustrates the minimum air temperature used for calculating CDD and HDD, along with the inlet temperature displayed only when the GSHP is operational in the numerical model. This scenario, devoid of cooling demand, evaluates the short- and long-term energy performance of the CSM system under conditions of elevated heating demand. Fig. 9(b) presents the maximum air temperature used for evaluating CDD and HDD. This scenario, incorporating both heating and cooling demands, assesses the energy performance of the CSM system under a more balanced distribution of heating and cooling requirements. Since the EDs are evaluated from actual air temperature values, the total number of CSM activation days for both cooling and heating demand varies each year in both EDs (see Fig. 9).

6. Numerical analysis to aid thermal design of a real application

To evaluate the energy performance of the CSM full-scale test, two distinct ED were simulated as detailed in Section 5. The first ED, Energy Demand 1 (ED1), was assessed using the minimum daily air temperature, resulting exclusively in heating demand, as illustrated in Fig. 9(a). The second demand, Energy Demand 2 (ED2), was evaluated using the highest daily air temperature, leading to a more balanced heating and cooling demand, as shown in Fig. 9(b). These simulations enable the assessment of the short-term and long-term thermal impacts on soil temperature and the system's energy performance for both heating and cooling scenarios.

To further understand the contribution of the connection pipes, which have a total length of 380.9 m, comprising nearly one-fourth of the total length of the U-loop pipes (1391.2 m), two additional simulations were conducted. In these simulations, the thermal conductivity of the connection pipes was set to 0.04 W/mK to simulate an insulation layer both for ED1 and ED2 scenarios, thereby minimising the energy extraction or injection from the connection pipes.

Finally, to better analyse the thermal interaction among all the U-loops, an additional simulation was conducted by simulating only half of the U-loops, with the horizontal distance between two consecutive U-loops increased from 1.1 m to 2.2 m.

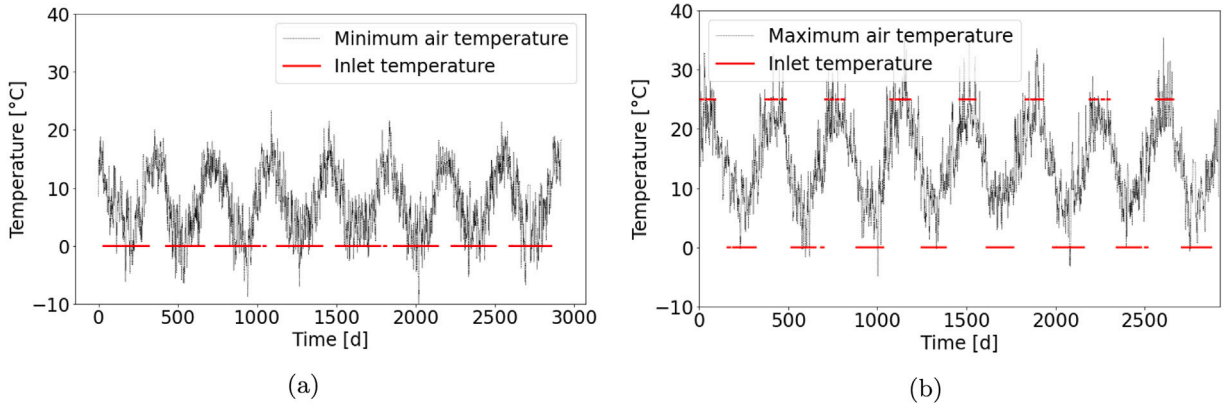

Fig. 9. Minimum and maximum daily air temperatures used to evaluate the EDs, along with the inlet temperature of the CSM wall loops. The inlet temperature is shown only when the CSM energy wall is operational: (a) minimum, and (b) maximum daily air temperature and the inlet temperature reflecting the ED.

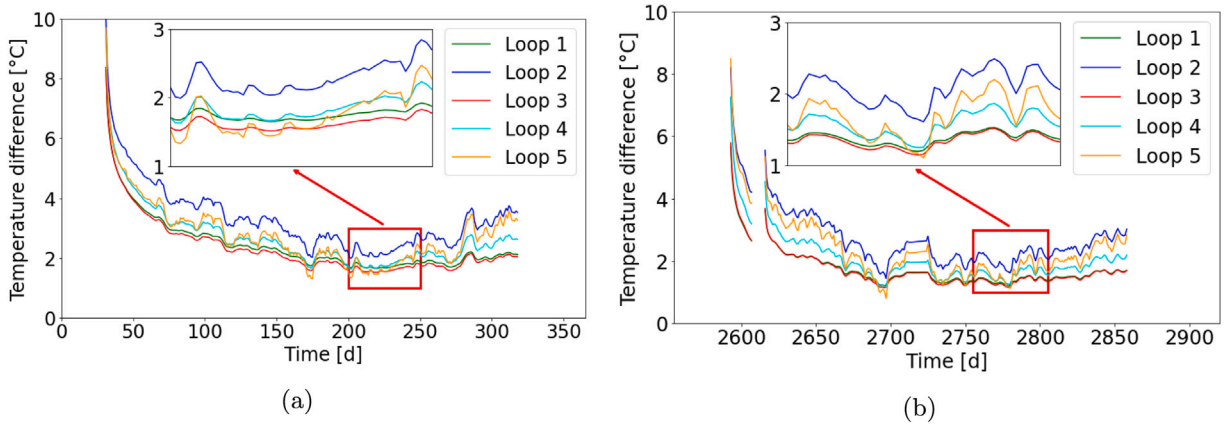

Fig. 10. Temperature difference between the inlet and outlet temperatures of the heat pump for each subgroup, measured during the (a) first, and (b) eighth years under the ED1 scenario.

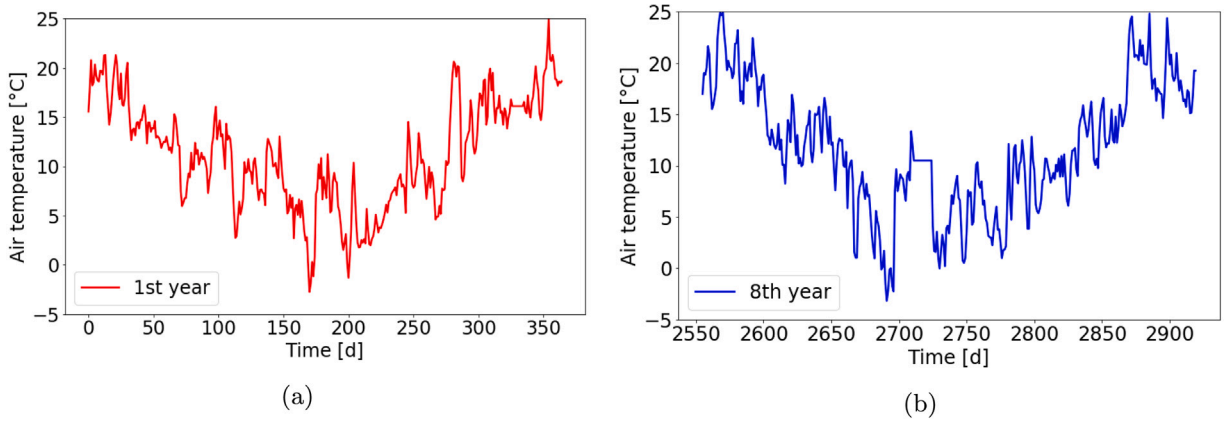

Fig. 11. Daily air temperature values simulated during the (a) first, and (b) eighth simulated years under the ED1 scenario.

6.1. Heating demand

Simulating the CSM system operation using ED1 involves applying a heavy heating demand over an 8-year period that can lead to the depletion of the heat source, as the soil temperature gradually decreases over time. Fig. 10 illustrates the temperature difference between the inlet and outlet of the heat pump during the 1st and 8th year of CSM system operation for each loop group, that are shown in Fig. 1. Similar to other geostructures embedded in the soil, the initial days of thermal activation exhibit higher temperature difference, which diminishes as the soil temperature decreases. After approximately one month, the temperature difference stabilises, indicating that a steady-state condition is gradually approached.

During the first year of operation, loops 1 and 3 exhibit a more constant temperature difference between the inlet and outlet of the heat pump compared to loops 2, 4, and 5 once a steady state is reached. This variation reflects the air temperature fluctuations over time, as shown in Fig. 11, which affect loops 2, 4, and 5 more significantly due to their

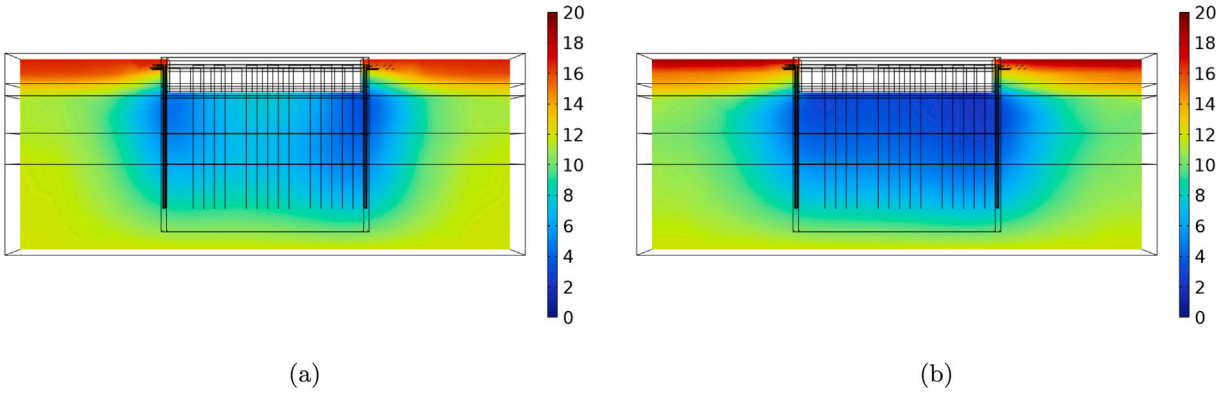

Fig. 12. Temperature distribution within the soil domain at the end of the (a) first, and (b) eighth years of simulation, depicted for a vertical cross-section intersecting the centre of the basement under the ED1 scenario.

longer connection pipes. The dependency on outside temperature is further evidenced by the last 30 days in both the 1st and 8th years, where the temperature difference increases with rising air temperatures. Loop 2 consistently shows the highest temperature difference during both the 1st and 8th years, attributable to its combined vertical pipe length of 286 m and connection pipe length of 89 m, resulting in the greatest total pipe length (375 m) and a setup that presents a higher average spacing between U-loops. Loop 5, with connection pipes measuring 125 m, almost half of the length of its vertical pipes (247.2 m), is more influenced by outside temperature variations: after 200 days, when the air temperature is approximately 0 °C, loop 5 exhibits the lowest temperature difference while after 250 days, with the rise in air temperature, loop 5 shows the second-highest temperature difference.

The temperature difference between the inlet and outlet of the heat pump for each loop decreases from the 1st to the 8th year. This reduction is linked to the gradual decline in soil temperature over the years, as illustrated in Fig. 12. At the end of the 1st year, the temperature near the CSM wall is low due to heat extraction, with slight thermal interaction between the left and right sides of the CSM indicated by temperature variations beneath the centre of the basement. This thermal interaction becomes more evident by the end of the 8th year, when the temperature beneath the centre of the basement is similar to that near the CSM wall. Under the conditions of ED1, the soil, when the system is off, does not have sufficient time to fully recover its temperature through natural conduction, leading to a decrease in soil temperature and consequently a reduction in the energy performance of the CSM wall over the years.

The heat extraction rate associated with ED1, depicted in Fig. 13, is determined by dividing the total power extracted from the five loops by the total surface area of the thermo-activated panels in the CSM system, which totals 765 m^2. Similar to the inlet–outlet temperature difference of the heat pump, the heat extraction rate varies across different years. Despite differences in the total number of CSM activation days, the heat extraction rate during the first 200 days of the 1st year is higher than in the 2nd and 8th years, with the latter two displaying similar values. This decline is attributed to the gradual decrease in soil temperature over time. After day 200, the heat extraction rate remains consistent across all years and is more influenced by ambient temperature than by soil temperature.

The total energy gained for each year is evaluated by multiplying the power gained by the corresponding time. To facilitate comparison of the total energy gained across the simulated years, these values are divided by the number of days the CSM energy wall is operational during each year. Fig. 14 illustrates the energy gained per day for the simulated years, along with the average air temperature on the days when the CSM system is operational. The highest energy gained per day occurs in the first year when the soil temperature is higher. From the 2nd to the 8th year, as the soil temperature decreases, the energy gained per day fluctuates in accordance with the average air temperature.

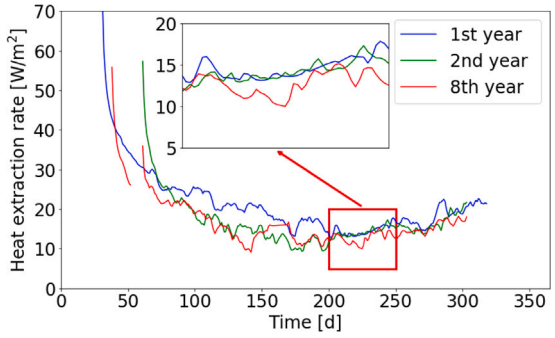

Fig. 13. Heat extraction rate during the first, second, and eighth years under the ED1 scenario.

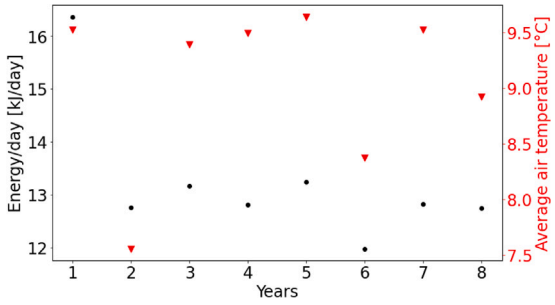

Fig. 14. Daily energy gain over the simulated years, correlated with the average air temperature measured on operational days only, under the ED1 scenario.

6.2. Heating and cooling demand

Assigning ED2 results in more constant temperature difference between the inlet and outlet of the heat pump over the years compared to ED1. In the heating scenario, as illustrated in Fig. 15, the temperature difference initially reaches approximately 10 °C and progressively decreases over time, stabilising at values consistently above 2 °C. This trend remains consistent across years and resembles the behaviour observed in the cooling scenario (Fig. 16). In contrast, the ED1 scenario exhibits lower temperature differences, particularly during the eighth year.

Despite loop 5 having the longest connection pipe, its short vertical loop does not reach the highly thermally conductive sand layer, which starts at a depth of 10.6 m, resulting in a lower temperature difference

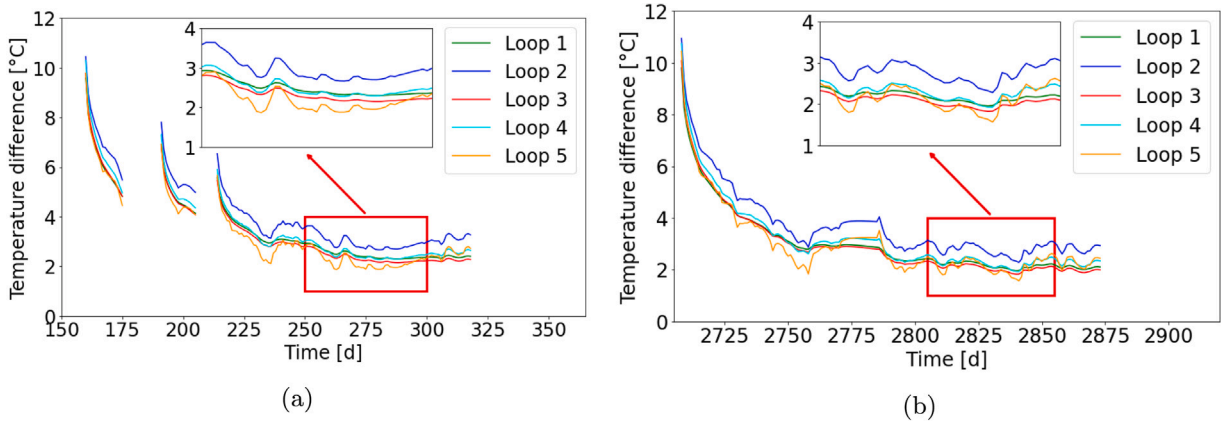

Fig. 15. Temperature difference between the inlet and outlet temperatures of the heat pump for each subgroup during the (a) first, and (b) eighth years under the heating demand-only condition of the ED2 scenario.

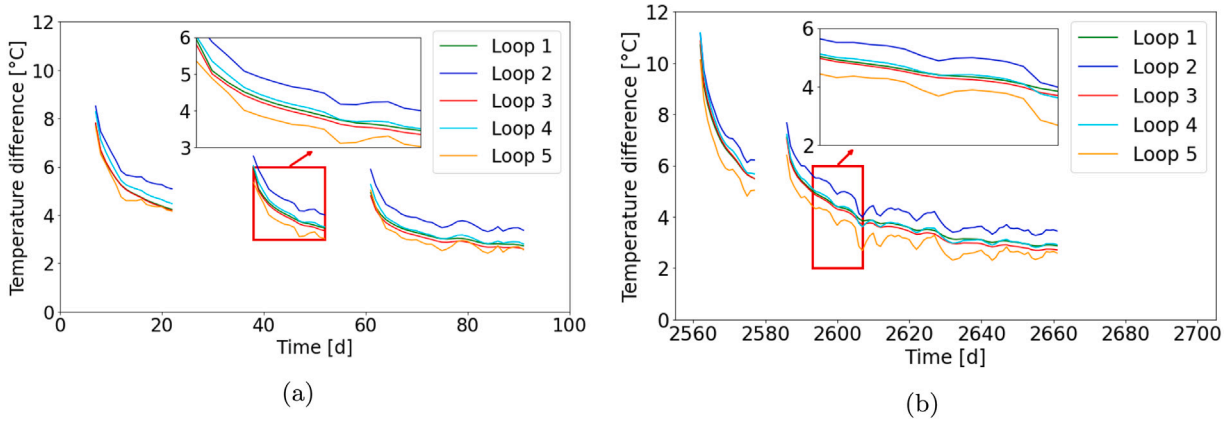

Fig. 16. Temperature difference between the inlet and outlet temperatures of the heat pump for each subgroup during the (a) first, and (b) eighth years under the cooling demand-only condition of the ED2 scenario.

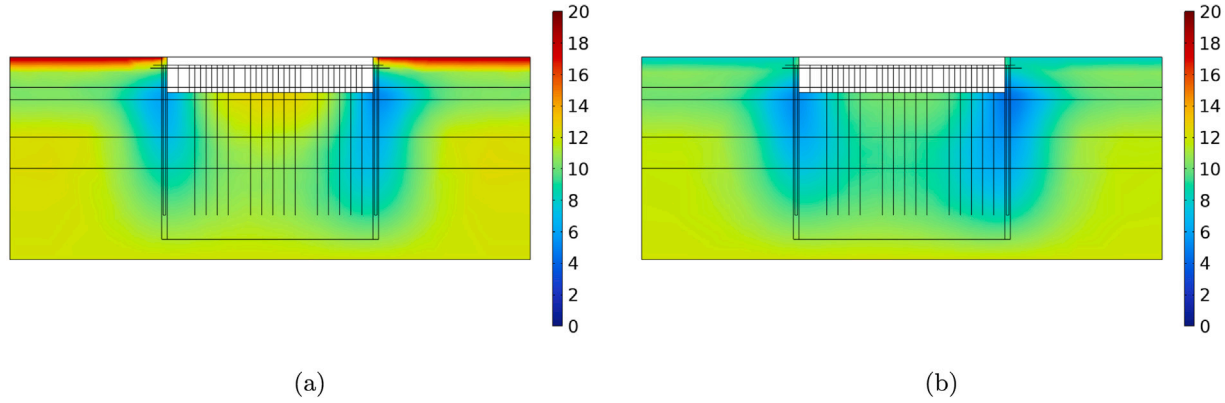

Fig. 17. Temperature distribution within the soil domain at the end of the (a) 1st, and (b) 8th years of simulation of the ED2 scenario.

for this loop compared to the other loops. Conversely, loop 2 exhibits the highest temperature difference, consistent with the ED1 scenario.

The ED2 scenario results in a long-term reduction in soil temperature, as indicated by the higher soil temperature near the CSM wall at the end of the 1st year compared to the end of the 8th year (Fig. 17). However, the presence of cooling demand mitigates this reduction.

The gradual decrease in soil temperature over time results in a corresponding decline in the rate of heat extraction, as illustrated in Fig. 15(b). Simultaneously, this trend enhances the performance of cooling demand, as depicted in Fig. 18.

Following the first year of simulation, the rates of heat extraction and injection stabilise, with the heat injection rate marginally surpassing the heat extraction rate. This difference is more evident in the daily energy gains during cooling demand versus heating demand, as demonstrated in Fig. 19.

6.3. Role of connection pipe

6.3.1. Energy demand 1

The role of the connection pipes was examined by comparing the energy performance of the system with and without insulated connection

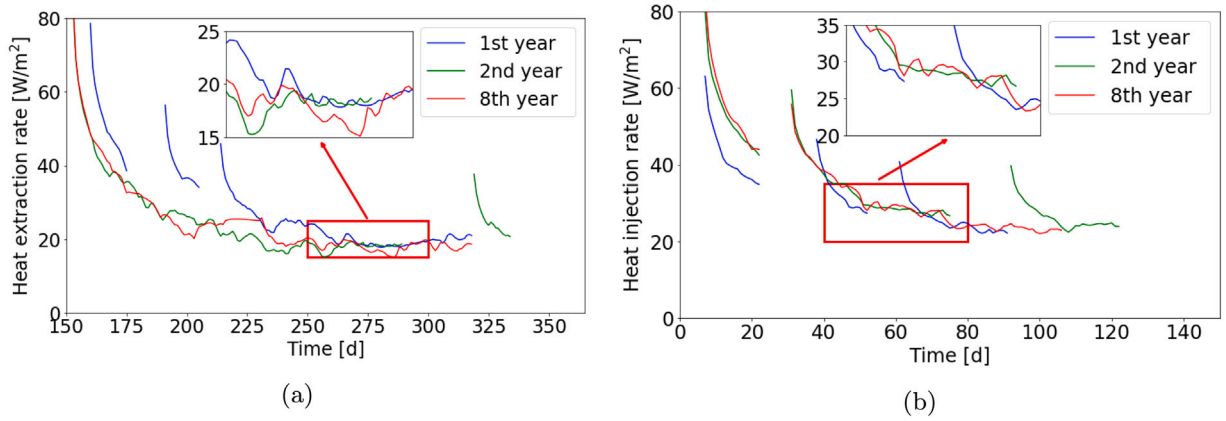

Fig. 18. Heat extraction rate trend through the years for (a) heating, and (b) cooling demand for the ED2 scenario.

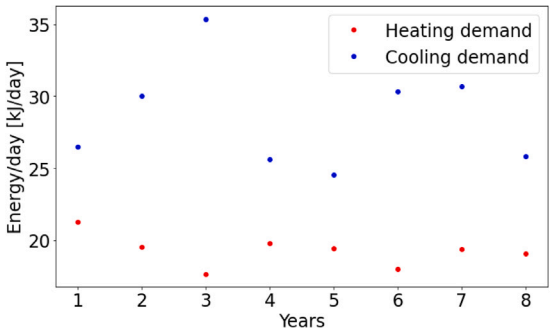

Fig. 19. Energy gained per day for the simulated years for heating and cooling demand under ED2 scenario.

pipes. Fig. 20 illustrates the temperature difference between the inlet and outlet of the heat pump during the 1st and 8th years of simulation with insulated connection pipes. Once steady state is reached, the temperature difference remains relatively constant, indicating a diminished impact of air temperature on the system's energy performance. Loop 5 exhibits the lowest temperature difference due to its short depth, which does not reach the deeper saturated sand layer with higher thermal properties. Conversely, loop 2 shows the highest temperature difference, slightly exceeding that of loops 1, 3, and 4. This is attributed to the vertical pipe configuration, where some U-loops in loop 2 have greater spacing compared to the other loops (see Fig. 1. Except for loop 5, the temperature differences for ED2 among the loops are lower than those for ED1 due to the reduced impact of the connection pipes.

During the first four years of simulation, the daily energy gained, as shown in Fig. 21, decreases each year before stabilising at a nearly constant value from years 4 to 8. The slight variations from year 4 to 8 are due to fluctuations in outside air temperature, which affect the shallow depth temperature profile, and the number of operational days per year.

On days when the air temperature is below the inlet temperature, the heat extraction rate with insulated connection pipes is nearly equal to that of non-insulated pipes, as illustrated in Fig. 22 with their difference shown in Fig. 23. Notably, during the first year, the heat extraction rate difference (Fig. 23(a)) remains consistently positive. However, by the eighth year (Fig. 23(b)), when air temperatures fall below 0 °C, the heat extraction rate difference exhibits negative values, indicating that a portion of the extracted heat is lost through the connection pipes. Furthermore, the difference in heat extraction rates is more pronounced in the 8th year, indicating that over time, more energy is extracted from the horizontal pipes compared to the vertical pipes due to the decrease in soil temperature.

The soil temperature at the end of the eighth year, as illustrated in Fig. 24, remains unchanged regardless of whether the connection pipes are insulated or not. This indicates that the integration of vertical and horizontal loops does not influence soil temperature under conditions of heating demand alone.

6.3.2. *Energy demand 2*

Similar to ED1, both the heat extraction rate and heat injection rate exhibit more stable trends and lower values when the connection pipes are insulated compared to when they are not under the ED2 scenario, as illustrated in Fig. 25.

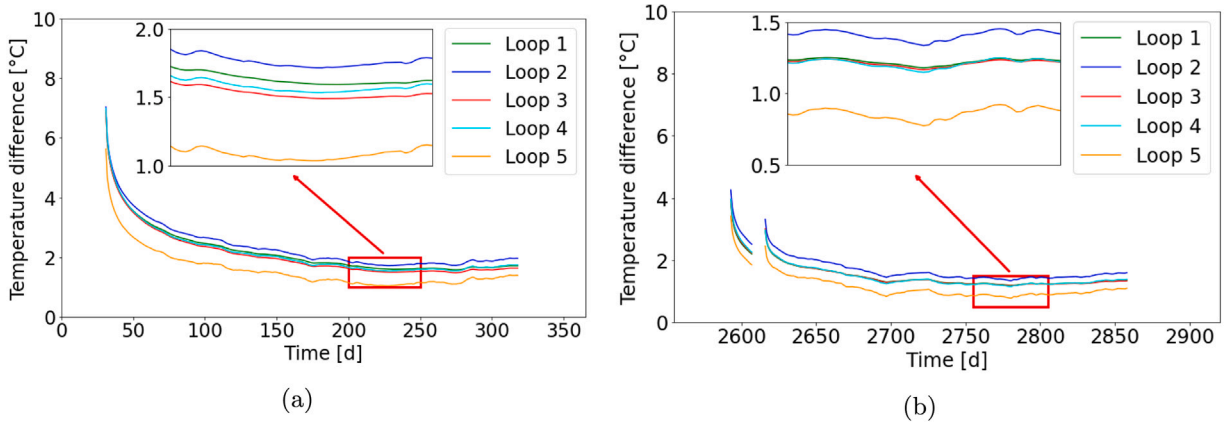

Fig. 20. Temperature difference between the inlet and the outlet temperature of the heat for each subgroup for the (a) 1st year, and (b) 8th year with insulated connection pipes.

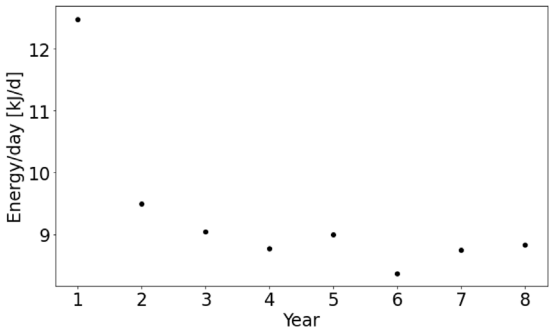

Fig. 21. Energy gained per day for the simulated years for heating and cooling demand under ED1 scenario and insulated connection pipes.

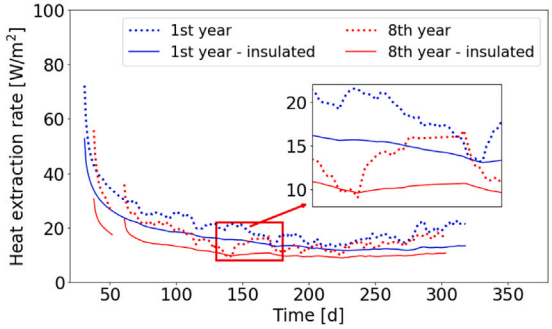

Fig. 22. Heat extraction rates for the 1st and 8th year of simulation under ED1 scenario and insulated connection pipes.

Regarding the heating demand, the heat extraction rate difference between insulated and non-insulated connection pipes during the 1st and 8th years, shown in Fig. 26, is on average lower than that evaluated for ED1. Even when the air temperature drops below the inlet temperature value, the heat extraction rate difference remains higher or equal to zero, whereas for ED1 it shows lower values.

Conversely, the heat injection rate difference, depicted in Fig. 27, is lower than the heat extraction rate difference and shows less dependency on outside temperature. Additionally, the heat injection rate difference remains consistently higher than zero, even with air temperatures reaching up to 25 °C.

When both heating and cooling demands are considered, the soil temperature at the end of the 8th year of simulation, shown in Fig. 28, is not significantly affected by whether the connection pipes are insulated or not.

6.4. U-loops setup

To analyse the effect of thermal interactions on the CSM system performance, a modified U-loop configuration was simulated. Specifically, instead of using the real-world configuration of 10 to 12 U-loops per loop group, only 6 U-loops were considered, as depicted in Fig. 29. This adjustment reduces the total number of U-loops from 52 to 30 and increases their spacing from 1.1 m to 2.2 m. The activated area based on the amount of panels that contains one U-loop is equal to 445 m^2, that is 42% lower than the real setup.

6.4.1. Energy demand 1

Under ED1 scenario, the heat extraction rate of the modified U-loop setup is higher than that of the original setup, as depicted in Fig. 30. The difference between these two configurations is lower on the first days of system activation when the temperature of the soil is higher, gradually increasing over time until it reaches more stable values, as shown in Fig. 31. By the 8th year of simulation, when soil temperatures are lower and the connection pipes play a more significant role, the heat extraction rate difference is reduced. Notably, the heat extraction difference is primarily between 40% and 50%, indicating that the overall energy performance of the CSM system improves by reducing the number of U-loops, as thermal interaction between the loops decreases. However, the activated area for the two U-loop setup is different (445 m^2 of the half-loop setup compared to 765 m^2 of the real U-loop setup) and despite the higher heat extraction rate, the total energy gained is less than the one evaluated for the real setup.

6.4.2. Energy demand 2

Under ED2 scenario, the simulation with the reduced U-loop setup results in higher values for both heat extraction and heat injection rates, as shown in Fig. 32. Both the heat extraction rate difference and the heat injection rate difference are lower than those evaluated for ED1 (see Fig. 33), starting at values up to 10% on the first day and increasing to around 40% over the course of the year. This increment trend is similar in both the 1st and 8th years of simulation, indicating that it is influenced by the reduction in soil temperature over the year.

Thus, under ED2 scenario, the reduction in thermal interference from reducing the number of U-loops still enhances energy performance, but this gain is less significant than under ED1.

7. Conclusions

The CSM energy wall represents a novel type of EG capable of providing both heating and cooling. The first full-scale test installation was conducted in Amstelveen, the Netherlands, aiming to evaluate its energy performance potential. Laboratory tests were performed to determine the basic mechanical properties of the CSM material and parameters necessary for assessing the energy performance of the CSM

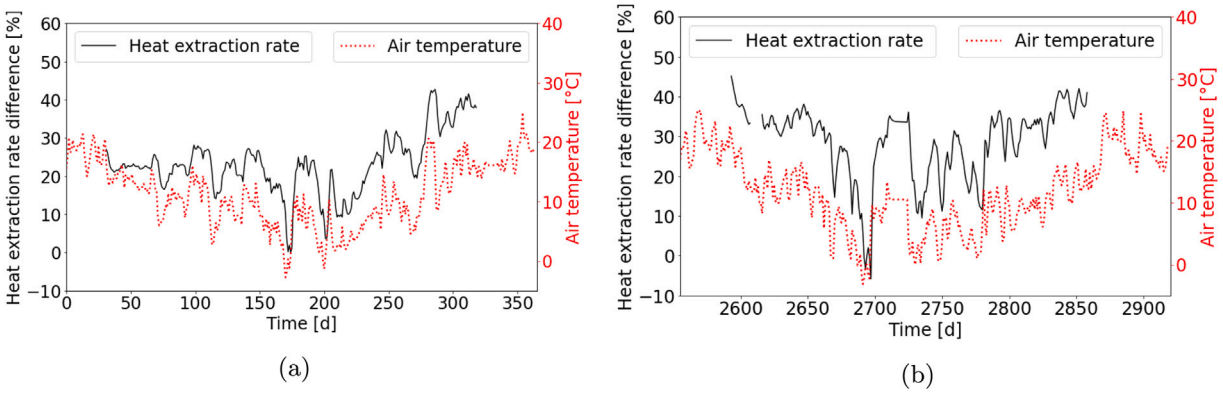

Fig. 23. Heat extraction rate difference between the non-insulated and insulated connection pipes for the (a) 1st year, and (b) 8th year under ED1 scenario.

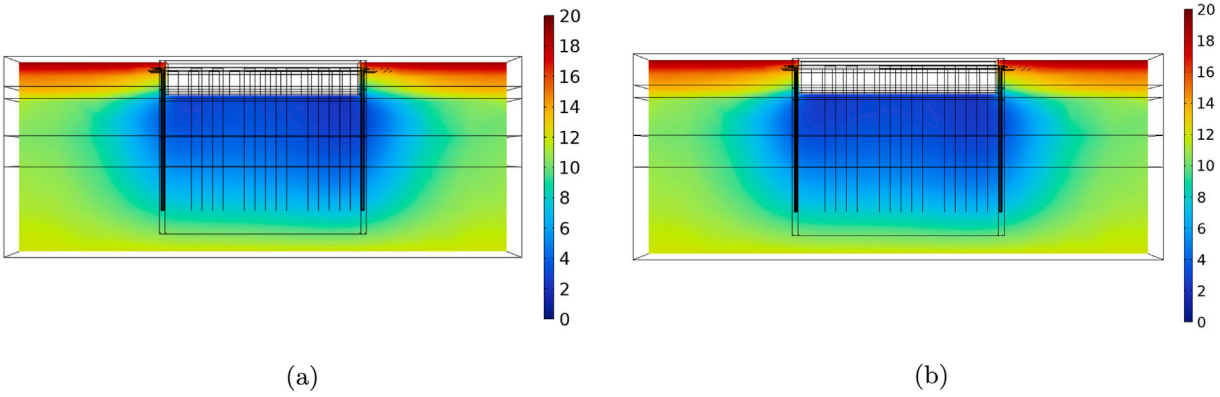

Fig. 24. Temperature profile within the soil comparison between the (a) not-insulated, and (b) insulated connection pipes at the end of the 8th year under ED1 scenario.

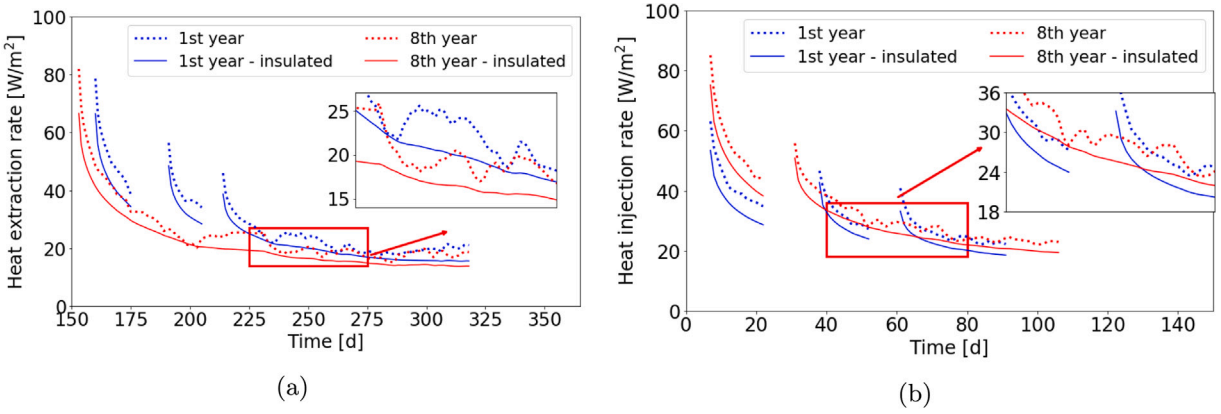

Fig. 25. Comparison between the temperature difference between the inlet and the outlet temperature of the heat pump for the not-insulated and insulated connection pipes for each subgroup for the 1st year and 8th year of simulation under ED2 scenario during (a) heating demand, and (b) cooling demand.

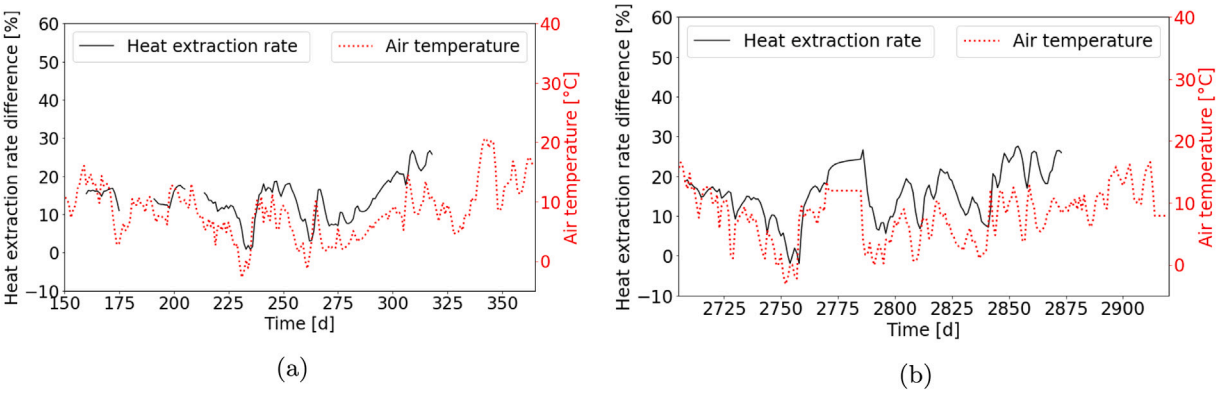

Fig. 26. Heat extraction rate difference between insulated and not-insulated connection pipes during the (a) 1st, and (b) 8th year of simulation compared to the air temperature values during heating demand only under ED2 scenario.

system and a detailed 3D FE numerical model of the full-scale test was developed to evaluate the heat exchange rate and the thermal activation effect on the soil temperature for both short-term and long-term scenario. The study focused on three main aspects: the impact of heating demand only versus both heating and cooling demands, the significance of uninsulated connection pipes in energy extraction/injection, and the influence of the U-loop setup on the heat exchange rate.

The main findings are:

- The amount of cement in the CSM material is low compared to the amount of soil. The homogeneity of density, thermal conductivity, and heat capacity of the CSM material results from soil mixing during installation rather than from a large presence of cement. This consistency is also reflected in the results of the unconfined compression tests.
- The building's energy demand affects both short-term and long-term energy performance of the CSM system. Specifically, the presence of both heating and cooling demands leads to a higher heat exchange rate over the years compared to heating demand only.
- In the heating demand only scenario, the heat exchange rate of subgroups with the longest connection pipes exhibits daily variations that mirror air temperature fluctuations. In the heating and

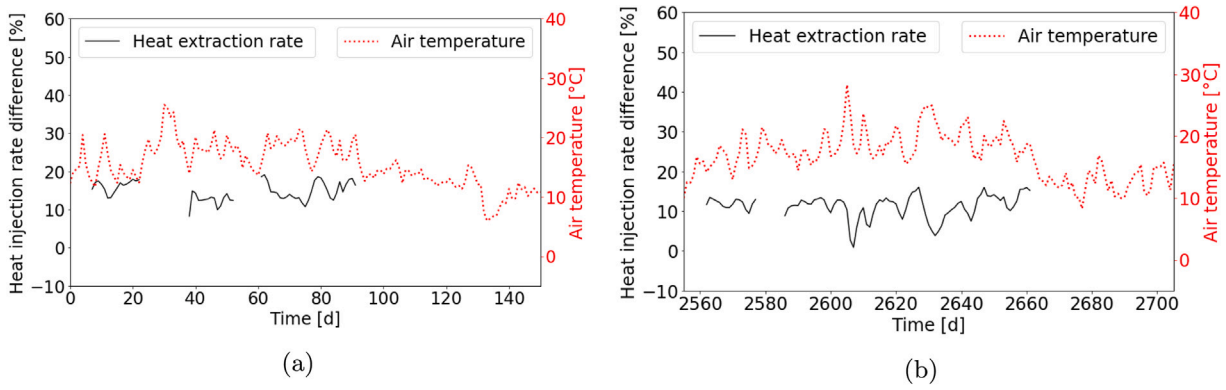

Fig. 27. Heat extraction rate difference between the insulated and not-insulated connection pipes during the (a) 1st, and (b) 8th year of simulation compared to the air temperature values during cooling demand only under ED2 scenario.

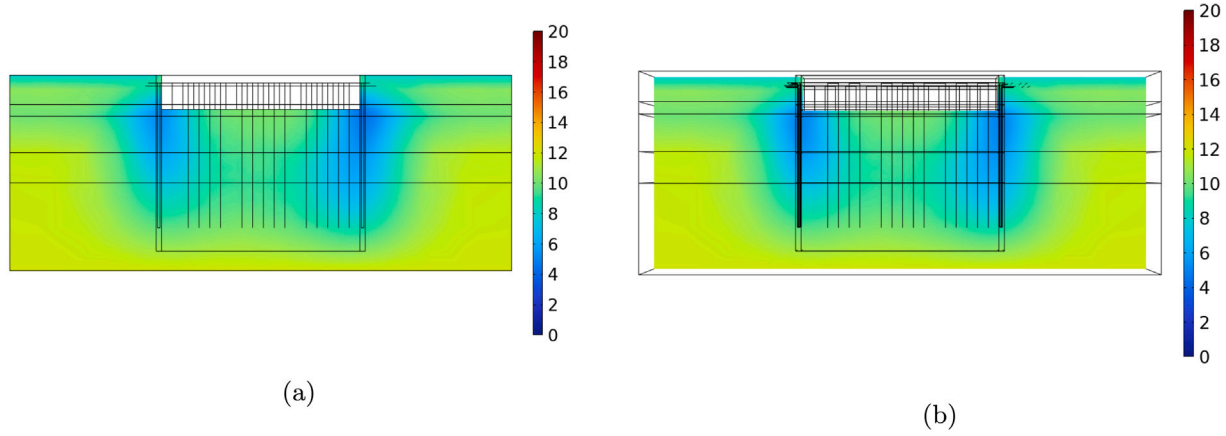

Fig. 28. Temperature distribution into the soil comparison between (a) not-insulated, and (b) insulated connection pipes and the end of the 8th year of simulation under ED2 condition.

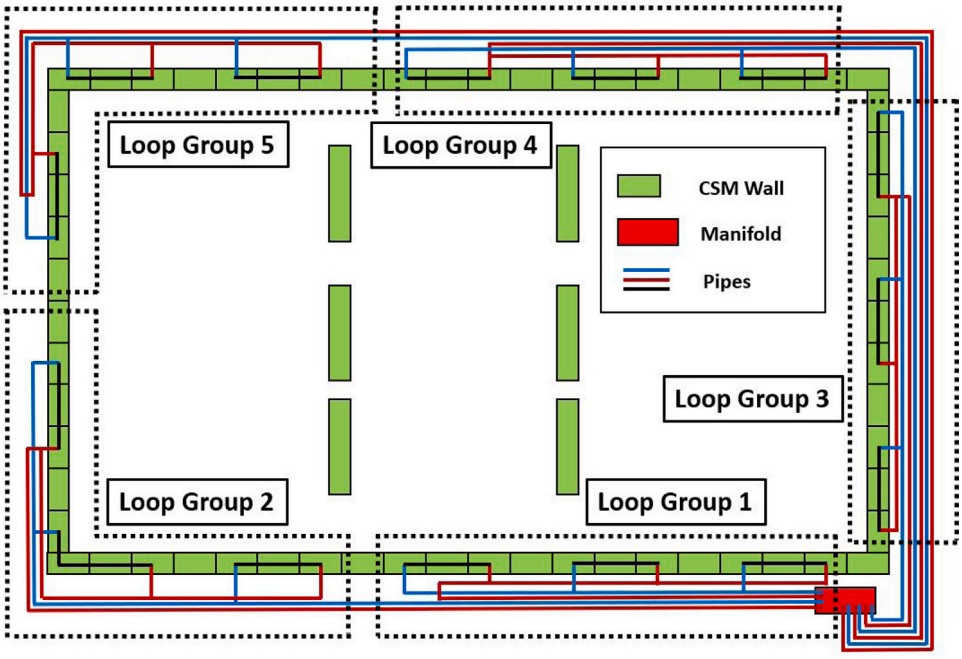

Fig. 29. Modified U-loops setup with the reduced number of U-loop.

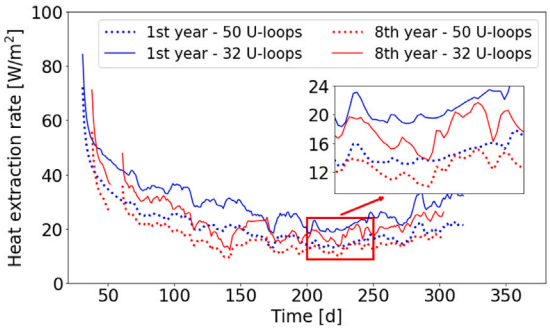

Fig. 30. Heat extraction rates comparison between the real and the modified U-loops setup for the 1st and 8th year of simulation under ED1 scenario.

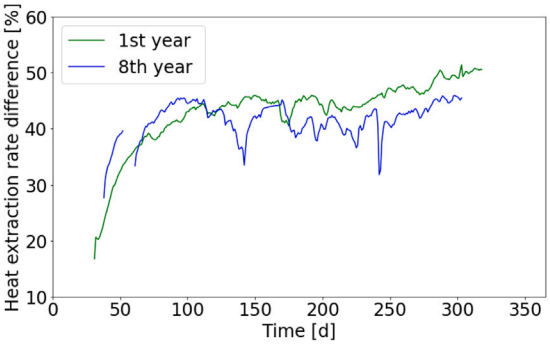

Fig. 31. Heat extraction rate difference between the real and the modified U-loops setup for the 1st and 8th year of simulation under ED1 scenario.

cooling scenario, this dependency is less pronounced, resulting in more stable energy performance over time.

- Non-insulated connection pipes increase the overall heat exchange rate of the system. This increase is more significant in the heating demand only scenario and can range from nearly zero when the air temperature is lower than the inlet temperature to up to 40% in heating demand only or 30% in both heating and cooling demand scenarios.
- In the heating demand only scenario, non-insulated connection pipes reduce the soil temperature decrease over time. This is not observed in heating and cooling scenarios, where soil temperature variations remain almost constant over time.
- Reducing the number of U-loops installed within the CSM wall decreases thermal interaction between U-loops and increases both heat extraction and injection rates for activated area. This increase can reach up to 50% in the heating demand only scenario and up to 40% in the heating and cooling scenarios, yet results in lower overall heat extraction/injection.

The CSM energy wall can be generally regarded as a viable geothermal solution, comparable to other EGs types, as it eliminates the need for dedicated installations and can provide significant amounts of renewable energy for space heating and cooling purposes. Further research is recommended, including experimental investigations of the CSM energy wall under varying climatic and geotechnical conditions, as well as the evaluation of associated thermo-mechanical effects.

CRediT authorship contribution statement

Marco Gerola: Writing – review & editing, Visualization, Software, Investigation, Writing – original draft, Validation, Methodology, Formal analysis, Conceptualization, Data curation. **Vincent Leclercq:** Methodology, Writing – review & editing, Conceptualization. **Philip J. Vardon:** Writing – review & editing, Conceptualization, Methodology. **Francesco Cecinato:** Writing – review & editing, Methodology, Supervision, Conceptualization.

Declaration of Generative AI and AI-assisted technologies in the writing process

During the preparation of this work the author(s) used ChatGPT in order to improve language and readability. After using this tool/service, the authors reviewed and edited the content as needed and take(s) full responsibility for the content of the publication.

Declaration of competing interest

The authors declare that they have no known competing financial interests or personal relationships that could have appeared to influence the work reported in this paper.

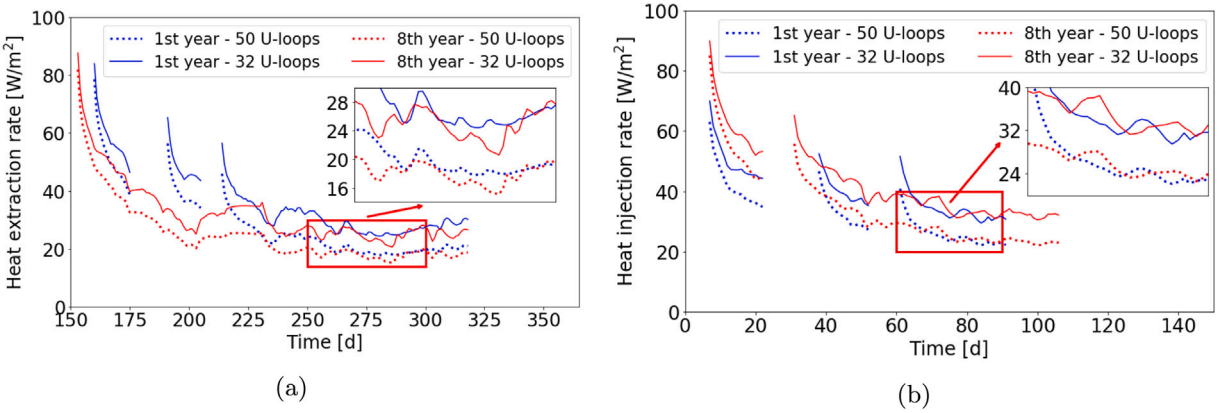

Fig. 32. Heat extraction rates comparison between the real and the modified hydraulic setup for the 1st and 8th year of simulation for the (a) heating demand, and (b) cooling demand under ED2 scenario.

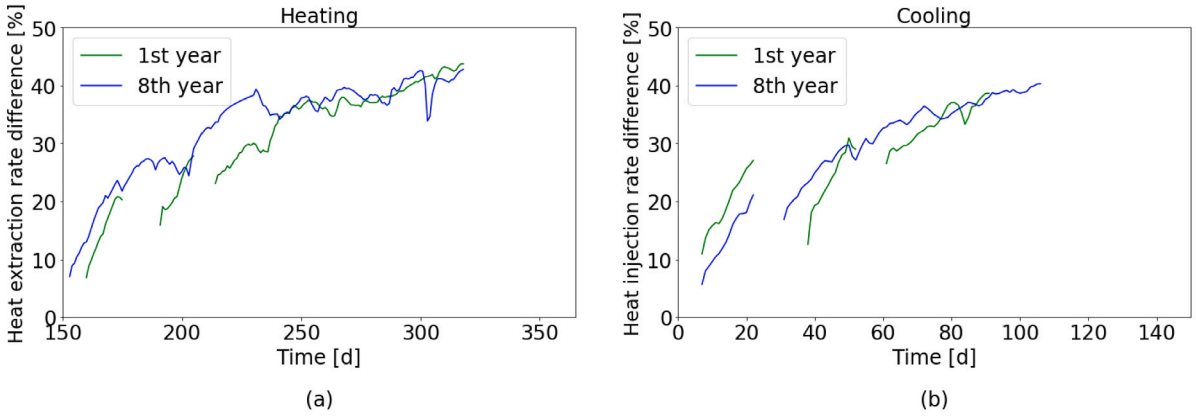

Fig. 33. Heat extraction/injection rate difference between the real and the modified hydraulic setup for the 1st and 8th year of simulation for the (a) heating demand, and (b) cooling demand under ED2 scenario.

Acknowledgements

M. Gerola and F. Cecinato acknowledge support under the PRIN (Italian Ministry of University and Research) program "Closing Knowledge Gaps On Energy Geostructures For Retrofitting Of Buildings And Infrastructures (GEOREFIT)". Support under the Italian Ministry of University's "PON - DM 1061/2021" scheme, co-funded by CRUX Engineering BV and the Kansen voor West S.P.O.E.D. project KvW3-00036 is also gratefully acknowledged.

Data availability

Data will be made available on request.

References

Adam, D., Markiewicz, R., 2009. Energy from earth-coupled structures, foundations, tunnels and sewers. Géotechnique 59 (3), 229–236. http://dx.doi.org/10.1680/geot.2009.59.3.229.

Adinolfi, M., Rianna, G., Mercogliano, P., Maiorano, R.M.S., Aversa, S., 2020. Behaviour of energy piles under climate-change scenarios: A case study in Southern Italy. Environ. Geotech. 8, 571–585. http://dx.doi.org/10.1680/jenge.19.00093.

Amatya, B., Soga, K., Bourne-Webb, P., Amis, T., Laloui, L., 2012. Thermo-mechanical behaviour of energy piles. Géotech. 62 (6), 503–519. http://dx.doi.org/10.1680/geot.10.P.116.

Amis, A., Loveridge, F., 2014. Energy piles and other thermal foundations for GSHP–developments in UK practice and research. Rehva J. 2014, 32–35.

Amis, T., Robinson, C., Wong, S., 2010. Integrating geothermal loops into the diaphragm walls of the Knightsbridge Palace Hotel project. Basements Undergr. Struct..

Angelotti, A., Sterpi, D., 2018. On the performance of energy walls by monitoring assessment and numerical modelling: a case in Italy. Environ. Geotech. 7 (4), 266–273. http://dx.doi.org/10.1680/jenge.18.00037.

Arnold, M., Beckhaus, K., Wiedenmann, U., 2011. Cut-off wall construction using Cutter Soil Mixing: a case study. Geotechnik 34 (1), 11–21. http://dx.doi.org/10.1002/gete.201000021.

Brandl, H., 2006. Energy foundations and other thermo-active ground structures. Geotech. 56 (2), 81–122. http://dx.doi.org/10.1680/geot.2006.56.2.81.

Broder, J., Preston, R., 2011. Chapter 1 - Imaging the head and brain. In: Broder, J. (Ed.), Diagnostic Imaging for the Emergency Physician. W.B. Saunders, Saint Louis, pp. 1–45. http://dx.doi.org/10.1016/B978-1-4160-6113-7.10001-8.

Busby, J., Kingdon, A., Williams, J., 2011. The measured shallow temperature field in Britain. Q. J. Eng. Geol. Hydrogeol. 44, 373–387. http://dx.doi.org/10.1144/1470-9236/10-049.

COMSOL, 2021. COMSOL Multiphysics User's Guide, Version 6.0. COMSOL.

Cvitan, L., Jurković, R.S., 2016. Secular trends in monthly heating and cooling demands in Croatia. Theor. Appl. Climatol. 125, 565–581. http://dx.doi.org/10.1007/s00704-015-1534-7.

Dalla Santa, G., Galgaro, A., Sassi, R., Cultrera, M., Scotton, P., Mueller, J., Bertermann, D., Mendrinos, D., Pasquali, R., Perego, R., Pera, S., Di Sipio, E., Cassiani, G., Carli, M.D., Bernardi, A., 2020. An updated ground thermal properties database for GSHP applications. Geotherm. 85, 101758. http://dx.doi.org/10.1016/j.geothermics.2019.101758.

Di Donna, A., Barla, M., Amis, T., 2017a. Energy geostructures: Analysis from research and systems installed around the world. In: DFI 2017: 42nd Annual Conference on Deep Foundations. pp. 1–11.

Di Donna, A., Cecinato, F., Loveridge, F., Barla, M., 2017b. Energy performance of diaphragm walls used as heat exchangers. Proc. Inst. Civ. Eng.-Geotech. Eng. 170 (3), 232–245. http://dx.doi.org/10.1680/jgeen.16.00092.

Di Donna, A., Laloui, L., 2015. Numerical analysis of the geotechnical behaviour of energy piles. Int. J. Numer. Anal. Methods Geomech. 39, 861–888. http://dx.doi.org/10.1002/nag.2341.

Di Donna, A., Loveridge, F., Piemontese, M., Barla, M., 2021. The role of ground conditions on the heat exchange potential of energy walls. Geomech. Energy Environ. 25, 100199. http://dx.doi.org/10.1016/j.gete.2020.100199.

Fillion, M.-H., Côté, J., Konrad, J.-M., 2011. Thermal radiation and conduction properties of materials ranging from sand to rock-fill. Can. Geotech. J. 48 (4), 532–542. http://dx.doi.org/10.1139/t10-093.

Fiorotto, R., Schöpf, M., Stötzer, E., 2005. Cutter soil mixing (CSM)-an innovation in soil mixing for creating cut-off and retaining walls. In: Proceedings of the 16th International Conference on Soil Mechanics and Geotechnical Engineering. IOS Press, pp. 1185–1188. http://dx.doi.org/10.3233/978-1-61499-656-9-1185.

Gerola, M., Cecinato, F., Leclercq, V., Vardon, P.J., 2025. Energy quay walls: Performance analysis and optimisation. Geomech. Energy Environ. 42, 100664. http://dx.doi.org/10.1016/j.gete.2025.100664.

Gerola, M., Lupattelli, A., Cecinato, F., Salciarini, D., Arola, T., 2023. Numerical Analysis of the Behaviour of Energy Micropiles Used for Heat Storage: A Case Study in Turku (Finland). Springer Science and Business Media Deutschland GmbH, Berlin/Heidelberg, Germany, pp. 808–815. http://dx.doi.org/10.1007/978-3-031-34761-0_97.

Hillel, D., 1982. Introduction to Environmental Soil Physics. Academic Press, San Diego, Calif..

Kavanaugh, S., 2010. An instruction guide for using a design tool for vertical ground-coupled, groundwater and surface water heat pumps systems—Ground source heat pump system designer, GshpCalc version 5.0. Energy information services, northport, AL. Energy Inf. Serv. Northport, AL, Accessed March 2015.

Kürten, S., Mottaghy, D., Ziegler, M., 2015. Design of plane energy geostructures based on laboratory tests and numerical modelling. Energy Build. 107, 434–444. http://dx.doi.org/10.1016/j.enbuild.2015.08.039.

Laloui, L., Rotta Loria, A.F., 2019. Analysis and Design of Energy Geostructures: Theoretical Essentials and Practical Application. Elsevier, Cambridge, http://dx.doi.org/10.1016/B978-0-12-816223-1.00017-5.

Laloui, L., Sutman, M., 2019. Energy geostructures: a new era for geotechnical engineering practice. In: Proc. XVII European Conference on Soil Mechanics and Geotechnical Engineering. pp. 1–15.

Leclercq, V., Gerola, M., Jong, D., Cecinato, F., de Kok, O., 2023. Cutter soil mix-energywall full-scale test experimental setup. In: Symposium on Energy Geotechnics 2023 Proceedings. TU Delft OPEN, pp. 1–2.

Lee, C.C., Chiu, Y.B., 2011. Electricity demand elasticities and temperature: Evidence from panel smooth transition regression with instrumental variable approach. Energy Econ. 33, 896–902. http://dx.doi.org/10.1016/j.eneco.2011.05.009.

Lewis, R.W., Schrefler, B.A., 1998. The Finite Element Method in the Static and Dynamic Deformation and Consolidation of Porous Media. Wiley, Chichester, UK.

Loveridge, F., McCartney, J.S., Narsilio, G.A., Sanchez, M., 2020. Energy geostructures: a review of analysis approaches, in situ testing and model scale experiments. Geomech. Energy Environ. 22, 100173. http://dx.doi.org/10.1016/j.gete.2019.100173.

Lund, J.W., Freeston, D.H., Boyd, T.L., 2011. Direct utilization of geothermal energy 2010 worldwide review. Geothermics 40 (3), 159–180. http://dx.doi.org/10.1016/j.geothermics.2011.07.004.

Makasis, N., Narsilio, G.A., 2020. Energy diaphragm wall thermal design: The effects of pipe configuration and spacing. Renew. Energy 154, 476–487. http://dx.doi.org/10.1016/j.renene.2020.02.112.

Matzarakis, A., Balafoutis, C., 2004. Heating degree-days over Greece as an index of energy consumption. Int. J. Climatol. 24, 1817–1828. http://dx.doi.org/10.1002/joc.1107.

Mimouni, T., Dupray, F., Laloui, L., 2013. On using tunnel anchors and bolts as heat exchangers with the ground. In: International EAGE Workshop on Geomechanics and Energy. pp. cp–369–00008. http://dx.doi.org/10.3997/2214-4609.20131945.

Moustris, K.P., Nastos, P.T., Bartzokas, A., Larissi, I.K., Zacharia, P.T., Paliatsos, A.G., 2015. Energy consumption based on heating/cooling degree days within the urban environment of Athens, Greece. Theor. Appl. Climatol. 122, 517–529. http://dx.doi.org/10.1007/s00704-014-1308-7.

Papakostas, K., Mavromatis, T., Kyriakis, N., 2010. Impact of the ambient temperature rise on the energy consumption for heating and cooling in residential buildings of Greece. Renew. Energy 35, 1376–1379. http://dx.doi.org/10.1016/j.renene.2009.11.012.

Petralli, M., Massetti, L., Orlandini, S., 2011. Five years of thermal intra-urban monitoring in Florence (Italy) and application of climatological indices. Theor. Appl. Climatol. 104, 349–356. http://dx.doi.org/10.1007/s00704-010-0349-9.

Rees, S.W., Adjali, M.H., Zhou, Z., Davies, M., Thomas, H.R., 2000. Thermal response prediction of a prototype energy micro-pile. Renew. Sustain. Energy Rev. 4, 213–265. http://dx.doi.org/10.1016/S1364-0321(99)00018-0.

Sanner, B., 2019. Summary of EGC 2019 Country Update Reports on Geothermal Energy in Europe. European Geothermal Congress 2019 Den Haag, pp. 11–14.

Scapin, S., Apadula, F., Brunetti, M., Maugeri, M., 2016. High-resolution temperature fields to evaluate the response of Italian electricity demand to meteorological variables: an example of climate service for the energy sector. Theor. Appl. Climatol. 125, 729–742. http://dx.doi.org/10.1007/s00704-015-1536-5.

Sterpi, D., Coletto, A., Mauri, L., 2017. Investigation on the behaviour of a thermo-active diaphragm wall by thermo-mechanical analyses. Geomech. Energy Environ. 9, 1–20. http://dx.doi.org/10.1016/j.gete.2016.10.001.

Sun, M., Xia, C., Zhang, G., 2013. Heat transfer model and design method for geothermal heat exchange tubes in diaphragm walls. Energy Build. 61, 250–259. http://dx.doi.org/10.1016/j.enbuild.2013.02.017.

Topolnicki, M., 2016. General overview and advances in deep soil mixing. In: XXIV Geotechnical Conference of Torino Design, Construction and Controls of Soil Improvement Systems. pp. 25–26.

Vardon, P.J., Gerola, M., Leclercq, V., de Jong, K., Haasnoot, J., Janssen, R., Stoelhorst, P., Pantev, I., de Vries, J., Bersan, S., et al., 2025. The energy quay wall: Results from a full-scale field test. Renew. Energy 253, 123552. http://dx.doi.org/10.1016/j.renene.2025.123552.

Vardon, P.J., Peuchen, J., 2021. CPT correlations for thermal properties of soils. Acta Geotech. 16, 635–646. http://dx.doi.org/10.1007/s11440-020-01027-2.

Xia, C., Sun, M., Zhang, G., Xiao, S., Zou, Y., 2012. Experimental study on geothermal heat exchangers buried in diaphragm walls. Energy Build. 52, 50–55. http://dx.doi.org/10.1016/j.enbuild.2012.03.054.

Zannin, J., Ferrari, A., Pousse, M., Laloui, L., 2021. Hydrothermal interactions in energy walls. Undergr. Space 6 (2), 173–184. http://dx.doi.org/10.1016/j.undsp.2020.02.001.